

Dynamic magnetic phase transition induced by parametric magnon pumping

Jun-Yi Shan,^{1,2,*} Jonathan B. Curtis,^{3,*} Mingyao Guo,^{1,2,*} Chang Jae Roh,^{4,5} C. R. Rotundu,⁶
Young S. Lee,^{6,7} Prineha Narang,³ Tae Won Noh,^{4,5} Eugene Demler,⁸ and D. Hsieh^{1,2,†}

¹*Department of Physics, California Institute of Technology, Pasadena, California 91125, USA*

²*Institute for Quantum Information and Matter, California Institute of Technology, Pasadena, California 91125, USA*

³*College of Letters and Science, University of California, Los Angeles, California 90095, USA*

⁴*Center for Correlated Electron Systems, Institute for Basic Science (IBS), Seoul 08826, Republic of Korea*

⁵*Department of Physics and Astronomy, Seoul National University (SNU), Seoul 08826, Republic of Korea*

⁶*Stanford Institute for Materials and Energy Sciences,*

SLAC National Accelerator Laboratory, Menlo Park, California 94025, USA

⁷*Department of Applied Physics, Stanford University, Stanford, California 94305, USA*

⁸*Institute for Theoretical Physics, ETH Zurich, 8093 Zurich, Switzerland*

(Dated: February 16, 2024)

Uncovering pathways to optically drive magnetic order-disorder transitions on ultrashort timescales can lead to the realization of novel out-of-equilibrium quantum phenomena. A long-sought pathway is to directly excite a highly non-thermal energy-momentum distribution of magnons, bypassing both charge and lattice degrees of freedom. However, this remains elusive owing to the weak coupling and large momentum mismatch between photons and magnons. Here we demonstrate strong parametric excitation of magnons across the entire Brillouin zone of the antiferromagnetic insulator $\text{Sr}_2\text{Cu}_3\text{O}_4\text{Cl}_2$ by periodically modulating the superexchange interaction with the electric field of light. The excitation efficiency is greatly enhanced by tuning to the van Hove singularity in the magnon spectrum, sufficient to transiently collapse the antiferromagnetic state using a pulsed laser field of 10^9 V/m. The order parameter recovery timescale increases by over 1000 times as a function of excitation density, reflecting a crossover from high- to low-energy magnon dominated decay dynamics. This electric-field induced parametric magnon pumping mechanism is applicable to a broad range of magnetic insulators and opens up the possibility of dynamically engineering magnon distributions by design.

I. Introduction

An extensively studied demagnetization pathway is through photo-thermal heating, whereby energy from a laser pulse is initially absorbed by the electronic or lattice subsystem and is subsequently transferred to the spin subsystem, raising the effective magnon temperature above the critical point [1–4]. This mechanism has been experimentally realized in many classes of materials ranging from ferromagnetic transition metals [5, 6], rare earth metals [7] and doped III-V semiconductors [8] to antiferromagnetic transition metal oxide Mott insulators [9]. However, owing to the thermal origin of magnon excitations, the demagnetization timescale is limited by the rate of heat exchange between subsystems.

A distinct pathway to ultrafast demagnetization is through non-thermal excitation of magnons. However, this has been challenging to realize for two main reasons. First, the coupling between light and spin is inherently weak [10]. Second, the magnon density of states is typically largest for momenta near the Brillouin zone boundary, which far exceeds the momentum of light in the optical frequency range. In magnetic insulators, large momentum magnons can be indirectly excited via magnon-phonon [11] and magnon-exciton [12–15] absorption processes, photo-doping [16–18], sub-wavelength confined optical fields [19] or extreme ultraviolet transient spin gratings [20]. However, while demagnetization can be

reached in some of these cases, magnon generation is accompanied by electronic or lattice excitations. An alternative approach is to directly excite magnons using light that is far detuned from any electronic or phonon resonances. Although directly excited single magnons are confined near the zone center [21–25], finite momentum magnons can be directly excited via two-magnon processes. One established process is parametric pumping, where a counter-propagating magnon pair is selectively excited at half the frequency of a microwave magnetic field [26–28]. Another process is second-order impulsive stimulated Raman scattering, where magnon pairs are simultaneously excited throughout the Brillouin zone by an oscillating electric field far off-resonant from two-magnon energies [29–31]. So far, however, none of these processes have been shown to generate sufficiently high magnon densities to cause demagnetization for fluences up to tens of mJ/cm^2 .

Here we demonstrate electric-field induced parametric pumping – a direct two-magnon excitation process allowed in locally non-centrosymmetric magnets – that enables both strong electric-dipole coupling and energy selectivity. Using the square-lattice cuprate antiferromagnetic Mott insulator $\text{Sr}_2\text{Cu}_3\text{O}_4\text{Cl}_2$ as a platform, we show that by selectively pumping a large non-thermal population of pure magnons around a van Hove singularity in the magnon spectrum located near the zone boundary, ultrafast demagnetization can be realized with pulsed fields

of 1.1×10^9 V/m (corresponding to a fluence $F = 19.2$ mJ/cm²).

II. Minimizing multiphoton charge excitation

The hierarchy of energy scales in copper-oxide based square lattice spin-1/2 Mott antiferromagnets is particularly suitable for demonstrating this phenomenon. Strong nearest-neighbor magnetic exchange interactions give rise to large magnon energies ($\hbar\omega_{\text{mag}}$) in the mid-infrared range, which is conducive to strong-field driving. Moreover, in certain compounds, the magnon bandwidth exceeds the phonon bandwidth by several times while the charge gap (Δ_g) exceeds twice the magnon bandwidth by several times. For $\text{Sr}_2\text{Cu}_3\text{O}_4\text{Cl}_2$, inelastic neutron scattering and Raman spectroscopy [32, 33] experiments report maximum magnon and phonon energies of approximately 0.3 eV and 0.08 eV, respectively. Our ellipsometry measurements show $\Delta_g = 1.86$ eV (Fig. 1a) [34]. This provides a large energy window for parametric magnon pumping that is far detuned from resonant electronic and lattice excitations.

Nevertheless, in the high field regime, charge excitations can still be made with pump photon energies ($\hbar\omega_{\text{pu}}$) below Δ_g via nonlinear processes such as multi-photon absorption and Zener tunneling [35, 36]. To verify the existence of an energy window across $2\hbar\omega_{\text{mag}}$ that is sufficiently transparent to nonlinear charge excitation, we performed time-resolved optical reflectivity measurements as a function of $\hbar\omega_{\text{pu}}$ on $\text{Sr}_2\text{Cu}_3\text{O}_4\text{Cl}_2$ single crystals. The probe photon energy was tuned near Δ_g to enhance sensitivity to photo-carrier population. For above-gap pumping ($\hbar\omega_{\text{pu}} = 2$ eV), the differential reflectivity transient ($\Delta R/R$) is clearly asymmetric about time $t = 0$ - the instant of pump probe overlap - characteristic of rapid photo-carrier generation followed by slower relaxation (Fig. 1b). Upon lowering $\hbar\omega_{\text{pu}}$ below Δ_g , the reflectivity transient gradually evolves to being perfectly symmetric about $t = 0$, mimicking the pump probe cross correlation. This signifies a purely coherent response due to pump field dressing of the electronic bands [37], with no measurable photo-carrier production. For a fixed pump fluence of $F = 8.0$ mJ/cm², we find that the crossover to a predominantly coherent lineshape occurs below $\hbar\omega_{\text{pu}} \sim 0.6$ eV, which is the threshold for three-photon absorption ($\Delta_g/3$). This crossover can also be clearly visualized by plotting the magnitude of $\Delta R/R$ at $t = 0$ (or the amplitude of the photo-carrier contribution to $\Delta R/R$) versus $\hbar\omega_{\text{pu}}$ (Fig. 1c), which exhibits a drop as the photo-carrier contribution to $\Delta R/R$ is suppressed below $\Delta_g/3$. These results are consistent with the Keldysh parameter $\hbar\omega_{\text{pu}}/(eE_{\text{pu}}\xi) > 2$ calculated using relevant experimental values (e is the electron charge, ξ is the electron-hole correlation length, and E_{pu} is the peak pump field strength), which locates the system in

the multiphoton dominated regime.

III. Energy-selective magnon pumping induced demagnetization

The structure of $\text{Sr}_2\text{Cu}_3\text{O}_4\text{Cl}_2$ consists of a stack of square-net layers similar to the parent compounds of high-temperature superconducting cuprates. However, at the center of every other plaquette of the conventional CuO_2 square-net (the Cu_{I} sublattice) there exists an additional Cu ion (the Cu_{II} sublattice), which removes the center of inversion located between neighboring Cu_{I} sites but preserves global inversion symmetry (Fig. 2a). The nearest-neighbor $\text{Cu}_{\text{I}}\text{-Cu}_{\text{I}}$ antiferromagnetic (AFM) exchange coupling ($J_1 = 130$ meV) exceeds that for $\text{Cu}_{\text{I}}\text{-Cu}_{\text{II}}$ and $\text{Cu}_{\text{II}}\text{-Cu}_{\text{II}}$ by over an order of magnitude. Therefore, the Cu_{I} sublattice orders at a much higher temperature ($T_{\text{N,I}} \approx 380$ K) compared to the Cu_{II} sublattice ($T_{\text{N,II}} \approx 40$ K) [38]. However, the interaction between the AFM ordered Cu_{I} sublattice and the paramagnetic Cu_{II} sublattice below $T_{\text{N,I}}$ induces a weak in-plane magnetization \mathbf{M} along one out of four possible $\text{Cu}_{\text{I}}\text{-Cu}_{\text{I}}$ bond directions [39], breaking the fourfold (C_4) rotational symmetry of the underlying square lattice (Fig. 2a).

A previous study [40] showed that the loss of rotational symmetry below $T_{\text{N,I}}$ activates a bulk magnetic-dipole (MD) optical second harmonic generation (SHG) process of the form $P_i(2\omega) = \chi_{ijk}^{\text{MD}} E_j(\omega) H_k(\omega)$. Here χ_{ijk}^{MD} is a time-reversal odd (c -type) susceptibility tensor that couples linearly to \mathbf{M} , $E_j(\omega)$ and $H_k(\omega)$ are the electric and magnetic fields of the incident probe light at frequency ω , $P_i(2\omega)$ is the polarization induced at the second harmonic, and the indices run through x , y , and z . Interference between this MD contribution and a temperature-independent time-reversal even (i -type) bulk electric-quadrupole (EQ) contribution produces a rotational anisotropy (RA) SHG pattern with C_1 symmetry (Fig. 2b), whose orientation is locked to \mathbf{M} . This provides a unique opportunity to measure the demagnetization dynamics of a cuprate Mott AFM (Cu_{I}) using time-resolved RA SHG.

We carried out time-resolved RA SHG measurements using a high-speed rotating scattering plane technique [41]. The fundamental probe photon energy was fixed at 1.55 eV while the pump photon energy was varied across the window over which multiphoton absorption is suppressed. Both pump and probe beams were focused within a single magnetic domain [34, 40]. Figure 2c shows the temperature-dependent intensity of the largest lobe in the RA SHG pattern - corresponding to the scattering plane angle $\varphi = 90^\circ$ (Fig. 2a) - in the absence of pumping. The emergence of a temperature-dependent MD contribution atop a temperature-independent EQ background is clearly observed below $T_{\text{N,I}}$. The pump

beam is then introduced with the sample held at $T = 300$ K. Figure 2d shows the instantaneous SHG intensity at $\varphi = 90^\circ$ as a function of time delay relative to a pump pulse with $\hbar\omega_{\text{pu}} = 0.50$ eV and $F = 19.2$ mJ/cm², plotted on the same intensity scale as Fig. 2c. At $t = 0$ there is an abrupt intensity drop from the equilibrium $T = 300$ K value down to the EQ background value, signifying a complete suppression of the MD contribution. Full collapse of the AFM state is further corroborated by instantaneous RA patterns acquired around $t = 0$, which show that only a C_4 symmetric EQ contribution remains (Fig. 2e). The absence of any measurable photo-carrier population (Fig. 2d inset) suggests that the demagnetization is driven entirely by non-thermal magnons [34]. We also note that the resolution limited (< 100 fs) demagnetization dynamics is consistent with the fast timescale associated with Cu_I - Cu_I exchange ($\hbar/J_1 \approx 30$ fs where \hbar is Planck's constant), but is incompatible with the slow timescale associated with Cu_I - Cu_II pseudo-dipolar coupling (≈ 200 ps) that is responsible for the finite \mathbf{M} [39]. This rules out the possibility that the pump pulse is merely suppressing \mathbf{M} by reducing the Cu_I - Cu_II coupling, in turn decreasing the canting angle of the magnetic moments, while leaving long-range AFM order of Cu_I intact.

To ascertain whether the non-thermal magnons are excited in pairs with energy selectivity, we performed pump photon energy dependent measurements. Figure 3a shows a linear spin-wave calculation for $\text{Sr}_2\text{Cu}_3\text{O}_4\text{Cl}_2$ based on a two-dimensional Heisenberg model that includes nearest- and next nearest-neighbor Cu_I - Cu_I exchange energies fitted to experiments on $\text{Sr}_2\text{Cu}_3\text{O}_4\text{Cl}_2$ and its closely related compounds $\text{Sr}_2\text{CuO}_2\text{Cl}_2$ and $\text{Ba}_2\text{Cu}_3\text{O}_4\text{Cl}_2$ [32, 34, 42, 43]. There are van Hove singularities at two distinct momenta in the Brillouin zone: a saddle point at $(-\pi/2a, -\pi/2a)$ and a maximum at $(0, -\pi/a)$ - where a is the Cu_I - Cu_I bond length - that gives rise to a magnon density of states (DOS) that diverges at $\hbar\omega_{\text{mag}} \approx 0.26$ eV and vanishes sharply above around 0.31 eV (Fig. 3b) [44]. The two-magnon absorption rate (Γ) depends on the magnon DOS at $\hbar\omega_{\text{pu}}/2$ according to Fermi's golden rule:

$$\Gamma = \sum_{\mathbf{k}} \frac{2\pi}{\hbar^2} | \langle 2\mathbf{M}(\mathbf{k}) | H_c | \mathbf{g} \rangle |^2 \delta(2\hbar\omega_{\text{mag}}(\mathbf{k}) - \hbar\omega_{\text{pu}}) \quad (1)$$

where the sum is over the Brillouin zone, $|\mathbf{g}\rangle$ is the magnetic ground state, $|2\mathbf{M}(\mathbf{k})\rangle$ is the state with a pair of magnons excited at momenta $\pm\mathbf{k}$, H_c is the light-spin coupling Hamiltonian, and $\delta(\cdot)$ is the Dirac delta function. Therefore, a signature of energy-selective magnon pair generation in $\text{Sr}_2\text{Cu}_3\text{O}_4\text{Cl}_2$ is a demagnetization efficiency that reaches a maximum when $\hbar\omega_{\text{pu}}/2$ coincides with the DOS peak. We measured SHG transients analogous to Fig. 2d over a range of $\hbar\omega_{\text{pu}}$ within the window where multiphoton absorption is suppressed, keeping

both the pump pulse duration and F (8.0 mJ/cm²) constant. The level of demagnetization near $t = 0$ is a clearly non-monotonic function of $\hbar\omega_{\text{pu}}$ (Fig. 3c) and exhibits a maximum near 0.55 eV (Fig. 3f) [34], consistent with twice the DOS peak. To make sense of the measured line shape, it is necessary to first understand the light-spin coupling mechanism that controls the matrix element in Eqn. (1).

IV. The electric-field induced parametric magnon pumping mechanism

Photo-excitation of magnon pairs in AFM insulators has been extensively studied in the context of Raman and infrared absorption spectroscopy. Three main mechanisms have been put forward [45]: (a) electric-dipole coupling mediated by spin-orbit interactions, (b) direct magnetic-dipole coupling, and (c) electric-dipole coupling realized through photo-assisted spin exchange [46]. Mechanism (a) is unlikely to be dominant in $\text{Sr}_2\text{Cu}_3\text{O}_4\text{Cl}_2$ owing to the weak spin-orbit coupling in cuprates. Mechanism (b) can also be ruled out because the magnetic-dipole Hamiltonian involves a dot product between the magnetic moment and the magnetic field of the pump light [34]. Yet there is no measurable change in the demagnetization efficiency as the angle (θ) of a linearly polarized pump beam (Fig. 2a) is varied with respect to the direction of ordered moments (Figs. 3d & e).

Mechanism (c) originates from a spin-dependent electric polarization for two-magnon excitations of the form:

$$\mathbf{P} = \sum_{\langle ij \rangle} \mathbf{\Pi}_{ij} \mathbf{S}_i \cdot \mathbf{S}_j \quad (2)$$

where the sum is over spins \mathbf{S} on neighboring sites i and j and $\mathbf{\Pi}_{ij}$ is a phenomenological vector coupling strength. By symmetry, $\mathbf{\Pi}_{ij}$ transforms like a vector and is therefore non-vanishing if the mid-point of the $\langle ij \rangle$ bond is not a crystallographic inversion center [46], which is the case for $\text{Sr}_2\text{Cu}_3\text{O}_4\text{Cl}_2$. We note that an overall inversion symmetry of the lattice does not dictate whether \mathbf{P} is vanishing or not [34]. This enables an electric-dipole coupling of light to $\pm\mathbf{k}$ magnon pairs of the form $H_c = -\mathbf{P} \cdot \mathbf{E}_{\text{pu}} \cos\omega_{\text{pu}}t$, even in the absence of spin-orbit coupling or global inversion symmetry breaking. Physically, this represents a parametric magnon pumping process. As the equilibrium Heisenberg Hamiltonian with superexchange J_1 is dressed by H_c , the effective exchange along the $\langle ij \rangle$ bond becomes $J_1 + \Delta J_{ij}(t) = J_1 - \mathbf{E}_{\text{pu}} \cdot \mathbf{\Pi}_{ij} \cos\omega_{\text{pu}}t$, imparting a time-periodic modulation of J_1 at the pump frequency. In the case where the pump photon is absorbed (as opposed to inelastically scattered), the two magnons are created exclusively at $\hbar\omega_{\text{mag}}(\pm\mathbf{k}) = \hbar\omega_{\text{pu}}/2$ by conservation of

energy and momentum (Fig. 3g) [34]. We note that there could also be an additional contribution to \mathbf{P} that is proportional to the pump field \mathbf{E}_{pu} [47]. However, this would result in a Hamiltonian term that is quadratic in \mathbf{E}_{pu} , corresponding to an inelastic Raman scattering process [48, 49] where the magnon pairs are excited at energies much smaller than $\hbar\omega_{\text{pu}}$, which is inconsistent with our resonant photon absorption process.

By re-writing Eqn. (2) in terms of magnon operators and taking into account the C_4 symmetry of the $\text{Sr}_2\text{Cu}_3\text{O}_4\text{Cl}_2$ lattice, the matrix element $|(2\mathbf{M}(\mathbf{k})|H_c|\mathbf{g})|^2$ can be shown to be proportional to $\sin^2 k_x a + \sin^2 k_y a$ [34]. Using this expression we find that the bi-magnon absorption coefficient, which scales like $\Gamma \times \hbar\omega_{\text{pu}}$, is independent of θ , in agreement with experiment (Fig. 3e). Moreover, the calculated $\hbar\omega_{\text{pu}}$ dependence [34], convolved with our experimental energy resolution function, agrees well with the measured demagnetization efficiency curve (Fig. 3f). Collectively these data support energy-selective parametric magnon pumping as the origin of the observed demagnetization.

V. Relaxation of the non-thermal magnon bath

Our parametric magnon pumping mechanism provides an opportunity to study out-of-equilibrium magnon dynamics starting from a well-defined non-thermal distribution, without the presence of other optically excited quasiparticles. Figure 4a shows SHG transients measured with $\hbar\omega_{\text{pu}} = 0.55$ eV in a weak magnon pumping regime where the order parameter reduction at $t = 0$ is relatively small (Fig. 4a inset). Here we observe complete recovery back to the $t < 0$ value on a fast timescale (τ_1) of several picoseconds. In contrast, upon entering a stronger magnon pumping regime where the demagnetization is more significant, a slow recovery component (τ_2) on the hundreds of picoseconds timescale emerges atop the τ_1 component, becoming increasingly dominant as the pump fluence approaches and crosses the threshold for full demagnetization (Fig. 4b).

These observations can be comprehensively explained as follows. High-energy magnon pairs at $\pm(k_x, k_y, k_z)$ are initially excited in the three-dimensional Brillouin zone along an iso-energetic surface at $\hbar\omega_{\text{pu}}/2$, which is highly anisotropic owing to the weak inter-layer exchange ($J_c \approx 10^{-4}J_1$) in $\text{Sr}_2\text{Cu}_3\text{O}_4\text{Cl}_2$ (Fig. 4c). These high-energy magnons then disappear primarily via three processes: (i) emission into the surrounding un-pumped regions; (ii) annihilation by scattering with optical phonons; or (iii) internal thermalization through anharmonic magnon-magnon interactions, leading to the decay of high-energy magnons to a quasi-thermal anisotropic distribution of low-energy magnons (Fig. 4c). Since all three processes generally occur on the timescale of a picosecond [16, 50, 51], we attribute the τ_1 component to the loss of

high-energy magnons. In contrast, owing to a drastically reduced phase space for low-energy magnon-phonon scattering, the low-energy magnons cool very slowly - on the timescale of a nanosecond in comparable layered AFM insulators [16]. Thus, we attribute the τ_2 component to cooling of the low-energy magnon distribution.

Theoretical models [52] suggest that the efficiency of process (iii) in the previous paragraph increases with the initial density of high-energy magnons. Therefore, the weak pumping regime is dominated by processes (i) and (ii). Here, the density of resulting low-energy magnons is too low to impart any measurable change in the order parameter, so no τ_2 component is detected. The observed increase in τ_1 with increasing pump fluence (Fig. 4d) possibly originates from a density dependent downward renormalization of J_1 [53–55], as higher magnon densities lead to lower precession frequencies thus slower dissipation, assuming a constant energy dissipated per precession period [50]. In the strong pumping regime, the τ_2 component becomes measurable owing to the higher efficiency of process (iii), with both its amplitude and timescale continuing to increase with pump fluence. Above the fluence ($F_c = 14$ mJ/cm²) where the initial density of high-energy magnons reaches the threshold for full demagnetization at $t = 0$, a small τ_1 component can still be resolved atop a large τ_2 component (see the $F = 16.0$ mJ/cm² curve in Fig. 4b). Upon reaching an even higher fluence ($F^* = 19$ mJ/cm²) the τ_1 component becomes negligible, indicating a second threshold where the density of low-energy magnons alone is sufficiently high to induce full demagnetization. The value of τ_2 becomes very large at F^* - far exceeding our measurement time window - potentially signaling a divergence due to critical slowing down at a quasi-thermal phase transition [34, 51] (Fig. 4e). We note that the magnon density continues to increase with fluence even above F_c because the transiently demagnetized state can still support short-range intra-layer AFM correlations and intra-layer paramagnons despite the absence of inter-layer coherence due to the pronounced exchange anisotropy of $\text{Sr}_2\text{Cu}_3\text{O}_4\text{Cl}_2$.

VI. Conclusion and outlook

The electric-field induced parametric magnon pumping phenomenon demonstrated here is expected to be active across a wide range of AFM insulators with broken local inversion symmetry. While local inversion is broken by the additional Cu_{II} sublattice in $\text{Sr}_2\text{Cu}_3\text{O}_4\text{Cl}_2$, it can also be broken by metal-ligand-metal bond buckling, which is a common feature of cuprates and transition metal oxides more generally. Provided the energy of van Hove singularities in the magnon spectrum is sufficiently detuned from electronic and phonon resonances, our protocol can be used to rapidly turn off magnetic order in these systems by directly engineering the magnon bath. Through

temporal and spectral shaping of the pump pulse, highly tailored non-thermal magnon distributions can be created, opening up new possibilities for realizing exotic collective phenomena beyond demagnetization [56], such as magnon Bose-Einstein condensation [26], topological magnonic states [57], and superconductivity mediated by drive-enhanced spin fluctuations [58, 59].

During the submission process, we became aware of another work [60] discussing resonant electric-field induced pumping of zone-edge magnons in hematite. However, this work was focused on modifying the magnon spectrum and did not report demagnetization.

Acknowledgements

We acknowledge discussions with P. A. Lee, K. L. Seyler, M. Ye, and L. Balents. This work is funded by ARO MURI Grant No. W911NF-16-1-0361 and the Brown Investigator Award, a program of the Brown Science Foundation. D.H. also acknowledges support for instrumentation from the Institute for Quantum Information and Matter, an NSF Physics Frontiers Center (PHY-1733907). E.D. acknowledges support from the SNSF project 200021.212899, and from the ARO grant “Control of Many-Body States Using Strong Coherent Light-Matter Coupling in Terahertz Cavities”. C.J.R. and T.W.N. acknowledge support from the Institute for Basic Science in Korea (Grant No. IBS-R009-D1). J.B.C. and P.N. acknowledge support from the DOE-QIS program (DE-SC0022277) and from the Quantum Science Center (QSC), a National Quantum Information Science Research Center of the U.S. Department of Energy (DOE). P.N. gratefully acknowledges support from the Gordon and Betty Moore Foundation grant number GBMF8048 and from the John Simon Guggenheim Memorial Foundation (Guggenheim Fellowship in Physics). The work at Stanford and SLAC in the Stanford Institute for Materials and Energy Sciences (SIMES) was supported by the U.S. Department of Energy (DOE), Office of Science, Basic Energy Sciences (BES), Materials Sciences and Engineering Division, under Contract No. DE-AC02-76SF00515.

* These authors contributed equally to this work.

† Corresponding author: dhsieh@caltech.edu

- [1] Andrei Kirilyuk, Alexey V Kimel, and Theo Rasing, “Ultrafast optical manipulation of magnetic order,” *Rev. Mod. Phys.* **82**, 2731 (2010).
- [2] B. Koopmans, G. Malinowski, F. Dalla Longa, D. Steiauf, M. Fähnle, T. Roth, M. Cinchetti, and M. Aeschli-mann, “Explaining the paradoxical diversity of ultrafast laser-induced demagnetization,” *Nat. Mater.* **9**, 259–265 (2010).
- [3] SL Johnson, Matteo Savoini, Paul Beaud, Gerhard Ingold, Urs Staub, Fabrizio Carbone, Luca Castiglioni, Matthias Hengsberger, and Jürg Osterwalder, “Watching ultrafast responses of structure and magnetism in condensed matter with momentum-resolved probes,” *Struct. Dyn.* **4**, 061506 (2017).
- [4] AV Kimel, RV Pisarev, J Hohlfeld, and Th Rasing, “Ultrafast quenching of the antiferromagnetic order in FeBO₃: Direct optical probing of the phonon-magnon coupling,” *Phys. Rev. Lett.* **89**, 287401 (2002).
- [5] Eric Beaupaire, J-C Merle, A Daunois, and J-Y Bigot, “Ultrafast spin dynamics in ferromagnetic nickel,” *Phys. Rev. Lett.* **76**, 4250 (1996).
- [6] Phoebe Tengdin, Wenjing You, Cong Chen, Xun Shi, Dmitriy Zusin, Yingchao Zhang, Christian Gentry, Adam Blonsky, Mark Keller, Peter M Oppeneer, *et al.*, “Critical behavior within 20 fs drives the out-of-equilibrium laser-induced magnetic phase transition in nickel,” *Sci. Adv.* **4**, eaap9744 (2018).
- [7] A. Vaterlaus, T. Beutler, and F. Meier, “Spin-lattice relaxation time of ferromagnetic gadolinium determined with time-resolved spin-polarized photoemission,” *Phys. Rev. Lett.* **67**, 3314–3317 (1991).
- [8] E Kojima, R Shimano, Y Hashimoto, S Katsumoto, Y Iye, and M Kuwata-Gonokami, “Observation of the spin-charge thermal isolation of ferromagnetic Ga_{0.94}Mn_{0.06}As by time-resolved magneto-optical measurements,” *Phys. Rev. B* **68**, 193203 (2003).
- [9] J. A. Johnson, T. Kubacka, M. C. Hoffmann, C. Vicario, S. de Jong, P. Beaud, S. Gröbel, S.-W. Huang, L. Huber, Y. W. Windsor, E. M. Bothschafter, L. Rettig, M. Ramakrishnan, A. Alberca, L. Patthey, Y.-D. Chuang, J. J. Turner, G. L. Dakovski, W.-S. Lee, M. P. Minitti, W. Schlotter, R. G. Moore, C. P. Hauri, S. M. Koolpayeh, V. Scagnoli, G. Ingold, S. L. Johnson, and U. Staub, “Magnetic order dynamics in optically excited multiferroic TbMnO₃,” *Phys. Rev. B* **92**, 184429 (2015).
- [10] A G Gurevich and G A Melkov, *Magnetization Oscillations and Waves* (CRC Press, 2020).
- [11] J. Lorenzana and G. A. Sawatzky, “Phonon assisted multimagnon optical absorption and long lived two-magnon states in undoped lamellar copper oxides,” *Phys. Rev. Lett.* **74**, 1867–1870 (1995).
- [12] Darrell Dean Sell, RL Greene, and Robert M White, “Optical exciton-magnon absorption in MnF₂,” *Phys. Rev.* **158**, 489 (1967).
- [13] JS Dodge, AB Schumacher, J-Y Bigot, DS Chemla, N Ingle, and MR Beasley, “Time-resolved optical observation of spin-wave dynamics,” *Phys. Rev. Lett.* **83**, 4650 (1999).
- [14] Davide Bossini, Kuniaki Konishi, Singo Toyoda, Takahisa Arima, Junji Yumoto, and Makoto Kuwata-Gonokami, “Femtosecond activation of magnetoelectricity,” *Nat. Phys.* **14**, 370–374 (2018).
- [15] Kenji Tsutsui, Kazuya Shinjo, Shigetoshi Sota, and Takami Tohyama, “Exciton-assisted low-energy magnetic excitations in a photoexcited Mott insulator on a square lattice,” *Commun. Phys.* **6**, 41 (2023).
- [16] M. P. M. Dean, Y. Cao, X. Liu, S. Wall, D. Zhu, R. Mankowsky, V. Thampy, X. M. Chen, J. G. Vale, D. Casa, Jungho Kim, A. H. Said, P. Juhas, R. Alonso-Mori, J. M. Glowia, A. Robert, J. Robinson, M. Sikorski, S. Song, M. Kozina, H. Lemke, L. Patthey, S. Owada, T. Katayama, M. Yabashi, Yoshikazu Tanaka,

- T. Togashi, J. Liu, C. Rayan Serrao, B. J. Kim, L. Huber, C.-L. Chang, D. F. McMorro, M. Först, and J. P. Hill, “Ultrafast energy- and momentum-resolved dynamics of magnetic correlations in the photo-doped Mott insulator Sr_2IrO_4 ,” *Nat. Mater.* **15**, 601–605 (2016).
- [17] Jih-An Yang, Nicholas Pellatz, Thomas Wolf, Rahul Nandkishore, and Dmitry Reznik, “Ultrafast magnetic dynamics in insulating $\text{YBa}_2\text{Cu}_3\text{O}_{6.1}$ revealed by time resolved two-magnon Raman scattering,” *Nat. Commun.* **11**, 2548 (2020).
- [18] Daniel G. Mazzone, Derek Meyers, Yue Cao, James G. Vale, Cameron D. Dashwood, Youguo Shi, Andrew J. A. James, Neil J. Robinson, Jiaqi Lin, Vivek Thampy, Yoshikazu Tanaka, Allan S. Johnson, Hu Miao, Ruitang Wang, Tadesse A. Assefa, Jungho Kim, Diego Casa, Roman Mankowsky, Diling Zhu, Roberto Alonso-Mori, Sanghoon Song, Hasan Yavas, Tetsuo Katayama, Makina Yabashi, Yuya Kubota, Shigeki Owada, Jian Liu, Junji Yang, Robert M. Konik, Ian K. Robinson, John P. Hill, Desmond F. McMorro, Michael Först, Simon Wall, Xuerong Liu, and Mark P. M. Dean, “Laser-induced transient magnons in $\text{Sr}_3\text{Ir}_2\text{O}_7$ throughout the brillouin zone,” *Proc. Natl. Acad. Sci. U.S.A.* **118**, e2103696118 (2021).
- [19] J. R. Hortensius, D. Afanasiev, M. Matthiesen, R. Leenders, R. Citro, A. V. Kimel, R. V. Mikhaylovskiy, B. A. Ivanov, and A. D. Caviglia, “Coherent spin-wave transport in an antiferromagnet,” *Nat. Phys.* **17**, 1001–1006 (2021).
- [20] Dmitriy Ksenzov, Alexei A. Maznev, Vivek Unnikandanunni, Filippo Bencivenga, Flavio Capotondi, Antonio Caretta, Laura Foglia, Marco Malvestuto, Claudio Masciovecchio, Riccardo Mancigrucci, Keith A. Nelson, Matteo Pancaldi, Emanuele Pedersoli, Lisa Randolph, Hendrik Rahmann, Sergei Urazhdin, Stefano Bonetti, and Christian Gutt, “Nanoscale Transient Magnetization Gratings Created and Probed by Femtosecond Extreme Ultraviolet Pulses,” *Nano Lett.* **21**, 2905–2911 (2021).
- [21] AV Kimel, A Kirilyuk, PA Usachev, RV Pisarev, AM Balbashov, and Th Rasing, “Ultrafast non-thermal control of magnetization by instantaneous photomagnetic pulses,” *Nature* **435**, 655–657 (2005).
- [22] Tobias Kampfrath, Alexander Sell, Gregor Klatt, Alexej Pashkin, Sebastian Mährlein, Thomas Dekorsy, Martin Wolf, Manfred Fiebig, Alfred Leitenstorfer, and Rupert Huber, “Coherent terahertz control of antiferromagnetic spin waves,” *Nat. Photonics* **5**, 31–34 (2011).
- [23] Evgeny A. Mashkovich, Kirill A. Grishunin, Roman M. Dubrovin, Anatoly K. Zvezdin, Roman V. Pisarev, and Alexey V. Kimel, “Terahertz light-driven coupling of antiferromagnetic spins to lattice,” *Science* **374**, 1608–1611 (2021).
- [24] Keita Yamaguchi, Makoto Nakajima, and Tohru Suetomo, “Coherent Control of Spin Precession Motion with Impulsive Magnetic Fields of Half-Cycle Terahertz Radiation,” *Phys. Rev. Lett.* **105**, 237201 (2010).
- [25] Dominik M. Juraschek, Derek S. Wang, and Prineha Narang, “Sum-frequency excitation of coherent magnons,” *Phys. Rev. B* **103**, 094407 (2021).
- [26] S. O. Demokritov, V. E. Demidov, O. Dzyapko, G. A. Melkov, A. A. Serga, B. Hillebrands, and A. N. Slavin, “Bose–Einstein condensation of quasi-equilibrium magnons at room temperature under pumping,” *Nature* **443**, 430–433 (2006).
- [27] Joe Bailey, Pavlo Sukhachov, Korbinian Baumgaertl, Simone Finizio, Sebastian Wintz, Carsten Dubs, Joerg Raabe, Dirk Grundler, Alexander Balatsky, and Gabriel Aeppli, “Multi-band Bose-Einstein condensate at four-particle scattering resonance,” (2022), arXiv:2201.11043 [cond-mat, physics:quant-ph].
- [28] Tony X. Zhou, Joris J. Carmiggelt, Lisa M. Gächter, Ilya Esterlis, Dries Sels, Rainer J. Stöhr, Chunhui Du, Daniel Fernandez, Joaquin F. Rodriguez-Nieva, Felix Büttner, Eugene Demler, and Amir Yacoby, “A magnon scattering platform,” *Proc. Natl. Acad. Sci. U.S.A.* **118**, e2019473118 (2021).
- [29] Jimin Zhao, A. V. Bragas, D. J. Lockwood, and R. Merlin, “Magnon Squeezing in an Antiferromagnet: Reducing the Spin Noise below the Standard Quantum Limit,” *Phys. Rev. Lett.* **93**, 107203 (2004).
- [30] D. Bossini, S. Dal Conte, Y. Hashimoto, A. Secchi, R. V. Pisarev, Th Rasing, G. Cerullo, and A. V. Kimel, “Macrospin dynamics in antiferromagnets triggered by sub-20 femtosecond injection of nanomagnons,” *Nat. Commun.* **7**, 10645 (2016).
- [31] Davide Bossini, Alexandra M Kalashnikova, Roman V Pisarev, Th Rasing, and Aleksei V Kimel, “Controlling coherent and incoherent spin dynamics by steering the photoinduced energy flow,” *Phys. Rev. B* **89**, 060405 (2014).
- [32] Joakim Holmlund, Christopher S. Knee, Jakob Andreasson, Mats Granath, A. P. Litvinchuk, and Lars Börjesson, “Two-magnon Raman scattering from the Cu_3O_4 layers in $(\text{Sr}_2, \text{Ba}_2)\text{Cu}_3\text{O}_4\text{Cl}_2$,” *Phys. Rev. B* **79**, 085109 (2009).
- [33] A. Zibold, H. L. Liu, S. W. Moore, J. M. Graybeal, and D. B. Tanner, “Optical properties of single-crystal $\text{Sr}_2\text{CuO}_2\text{Cl}_2$,” *Phys. Rev. B* **53**, 11734–11743 (1996).
- [34] See Supplemental Material. The Supplemental Material also contains Refs. [61–69].
- [35] Xinwei Li, Honglie Ning, Omar Mehio, Hengdi Zhao, Min-Cheol Lee, Kyungwan Kim, Fumihiko Nakamura, Yoshiteru Maeno, Gang Cao, and David Hsieh, “Keldysh Space Control of Charge Dynamics in a Strongly Driven Mott Insulator,” *Phys. Rev. Lett.* **128**, 187402 (2022).
- [36] Takashi Oka, “Nonlinear doublon production in a Mott insulator: Landau-Dykhne method applied to an integrable model,” *Phys. Rev. B* **86**, 075148 (2012).
- [37] Jun-Yi Shan, M. Ye, H. Chu, Sungmin Lee, Je-Geun Park, L. Balents, and D. Hsieh, “Giant modulation of optical nonlinearity by Floquet engineering,” *Nature* **600**, 235–239 (2021).
- [38] K Yamada, N Suzuki, and Jun Akimitsu, “Magnetic properties of $(\text{Sr}, \text{Ba})_2\text{Cu}_3\text{O}_4\text{Cl}_2$: two-dimensional antiferromagnetic cuprates containing two types of Cu-site,” *Phys. B: Condens. Matter* **213**, 191–193 (1995).
- [39] F. C. Chou, Amnon Aharony, R. J. Birgeneau, O. Entin-Wohlman, M. Greven, A. B. Harris, M. A. Kastner, Y. J. Kim, D. S. Kleinberg, Y. S. Lee, and Q. Zhu, “Ferromagnetic moment and spin rotation transitions in tetragonal antiferromagnetic $\text{Sr}_2\text{Cu}_3\text{O}_4\text{Cl}_2$,” *Phys. Rev. Lett.* **78**, 535–538 (1997).
- [40] K. L. Seyler, A. Ron, D. Van Beveren, C. R. Rotundu, Y. S. Lee, and D. Hsieh, “Direct visualization and control of antiferromagnetic domains and spin reorientation in a parent cuprate,” *Phys. Rev. B* **106**, L140403 (2022).
- [41] J. W. Harter, L. Niu, A. J. Woss, and D. Hsieh, “High-speed measurement of rotational anisotropy nonlinear

- optical harmonic generation using position-sensitive detection,” *Opt. Lett.* **40**, 4671 (2015).
- [42] M. Guarise, B. Dalla Piazza, M. Moretti Sala, G. Ghiringhelli, L. Braicovich, H. Berger, J. N. Hancock, D. van der Marel, T. Schmitt, V. N. Strocov, L. J. P. Ament, J. van den Brink, P.-H. Lin, P. Xu, H. M. Rønnow, and M. Grioni, “Measurement of magnetic excitations in the two-dimensional antiferromagnetic $\text{Sr}_2\text{CuO}_2\text{Cl}_2$ insulator using resonant x-ray scattering: Evidence for extended interactions,” *Phys. Rev. Lett.* **105**, 157006 (2010).
- [43] P. Babkevich, N. E. Shaik, D. Lançon, A. Kikkawa, M. Enderle, R. A. Ewings, H. C. Walker, D. T. Adroja, P. Manuel, D. D. Khalyavin, Y. Taguchi, Y. Tokura, M. Soda, T. Masuda, and H. M. Rønnow, “Magnetic excitations from the two-dimensional interpenetrating Cu framework in $\text{Ba}_2\text{Cu}_3\text{O}_4\text{Cl}_2$,” *Phys. Rev. B* **96**, 014410 (2017).
- [44] F. Bassani and G. Pastori Parravicini, *Electronic states and optical transitions in solids* (Pergamon Press, Oxford, 1975).
- [45] P. A. Fleury and R. Loudon, “Scattering of Light by One- and Two-Magnon Excitations,” *Phys. Rev.* **166**, 514–530 (1968).
- [46] Yukito Tanabe, Tôru Moriya, and Satoru Sugano, “Magnon-Induced Electric Dipole Transition Moment,” *Phys. Rev. Lett.* **15**, 1023–1025 (1965).
- [47] Anatolii E Fedianin, Alexandra M Kalashnikova, and Johan H Mentink, “Selection rules for ultrafast laser excitation and detection of spin correlation dynamics in a cubic antiferromagnet,” *Phys. Rev. B* **107**, 144430 (2023).
- [48] D Bossini, S Dal Conte, G Cerullo, O Gomonay, RV Pisarev, M Borovsak, D Mihailovic, J Sinova, JH Mentink, Th Rasing, *et al.*, “Laser-driven quantum magnonics and terahertz dynamics of the order parameter in antiferromagnets,” *Phys. Rev. B* **100**, 024428 (2019).
- [49] F Formisano, TT Gareev, DI Khusyainov, AE Fedianin, RM Dubrovin, PP Syrnikov, D Afanasiev, RV Pisarev, AM Kalashnikova, JH Mentink, *et al.*, “Coherent THz spin dynamics in antiferromagnets beyond the approximation of the Néel vector,” *APL Mater.* **12**, 011105 (2024).
- [50] Marija Djordjevic and Markus Münzenberg, “Connecting the timescales in picosecond remagnetization experiments,” *Phys. Rev. B* **75**, 012404 (2007).
- [51] A. de la Torre, Kyle L. Seyler, Michael Buchhold, Yuval Baum, Gufeng Zhang, Nicholas J. Laurita, John W. Harter, Liuyan Zhao, Isabelle Phinney, Xiang Chen, Stephen D. Wilson, Gang Cao, Richard D. Averitt, Gil Refael, and David Hsieh, “Decoupling of static and dynamic criticality in a driven Mott insulator,” *Commun. Phys.* **5**, 35 (2022).
- [52] Pavel E. Dolgirev, Marios H. Michael, Alfred Zong, Nuh Gedik, and Eugene Demler, “Self-similar dynamics of order parameter fluctuations in pump-probe experiments,” *Phys. Rev. B* **101**, 174306 (2020).
- [53] Tatuo Kawasaki, “Possibility of inverse Suhl instability processes by optical pumping in antiferromagnets,” *J. Magn. Reson.* (1969) **9**, 114–117 (1973).
- [54] Takashi Odagaki, “Photon pumped spin wave instability in rutile-type antiferromagnets,” *J. Phys. Soc. Jpn* **35**, 40–46 (1973).
- [55] Johan H Mentink and Martin Eckstein, “Ultrafast quenching of the exchange interaction in a mott insulator,” *Phys. Rev. Lett.* **113**, 057201 (2014).
- [56] Nicklas Walldorf, Dante M Kennes, Jens Paaske, and Andrew J Millis, “The antiferromagnetic phase of the Floquet-driven Hubbard model,” *Phys. Rev. B* **100**, 121110 (2019).
- [57] Daniel Malz, Johannes Knolle, and Andreas Nunnenkamp, “Topological magnon amplification,” *Nat. Commun.* **10**, 3937 (2019).
- [58] Jonathan B. Curtis, Andrey Grankin, Nicholas R. Poniatowski, Victor M. Galitski, Prineha Narang, and Eugene Demler, “Cavity magnon-polaritons in cuprate parent compounds,” *Phys. Rev. Res.* **4**, 013101 (2022).
- [59] Y. Wang, C.-C. Chen, B. Moritz, and T.P. Devereaux, “Light-enhanced spin fluctuations and *d*-wave superconductivity at a phase boundary,” *Phys. Rev. Lett.* **120**, 246402 (2018).
- [60] Christoph Schoenfeld, Lennart Feuerer, Dennis Wuhler, Wolfgang Belzig, Alfred Leitenstorfer, Dominik Juraschek, and Davide Bossini, “Dynamical renormalisation of a spin hamiltonian via high-order nonlinear magnonics,” *arXiv preprint arXiv:2310.19667* (2023).
- [61] Y. J. Kim, R. J. Birgeneau, F. C. Chou, M. Greven, M. A. Kastner, Y. S. Lee, B. O. Wells, A. Aharony, O. Entin-Wohlman, I. Ya. Korenblit, A. B. Harris, R. W. Erwin, and G. Shirane, “Neutron scattering study of $\text{Sr}_2\text{Cu}_3\text{O}_4\text{Cl}_2$,” *Phys. Rev. B* **64**, 024435 (2001).
- [62] Robert W. Boyd, *Nonlinear Optics* (Academic Press, Cambridge, 2020).
- [63] AV Kimel, CD Stanciu, PA Usachev, RV Pisarev, VN Gridnev, Andrei Kirilyuk, and Th Rasing, “Optical excitation of antiferromagnetic resonance in TmFeO_3 ,” *Phys. Rev. B* **74**, 060403 (2006).
- [64] M Matsubara, Y Okimoto, T Ogasawara, Y Tomioka, H Okamoto, and Y Tokura, “Ultrafast photoinduced insulator-ferromagnet transition in the perovskite manganite $\text{Gd}_{0.55}\text{Sr}_{0.45}\text{MnO}_3$,” *Phys. Rev. Lett.* **99**, 207401 (2007).
- [65] Hiroyuki Yada, Masakazu Matsubara, Hiroyuki Matsuzaki, Hiroyuki Yamada, Akihito Sawa, and Hiroshi Okamoto, “Discrimination between photodoping and heat-induced magnetization changes in $\text{Nd}_{0.52}\text{Sr}_{0.48}\text{MnO}_3$ using a heterostructure with SrTiO_3 ,” *Phys. Rev. B* **84**, 045114 (2011).
- [66] Masumi Ohno, Takayuki Kawamata, Megumi Akoshima, and Yoji Koike, “Thermal conductivity due to spins in the two-dimensional spin system $\text{Ba}_2\text{Cu}_3\text{O}_4\text{Cl}_2$,” *J. Phys. Soc. Jpn.* **88**, 064708 (2019).
- [67] S Noro, H Suzuki, and T Yamadaya, “Magnetic properties of $\text{Ba}_{2-x}\text{K}_x\text{Cu}_3\text{Cl}_2$,” *Solid State Commun.* **76**, 711–713 (1990).
- [68] H. Y. Hwang, P. Dai, S-W. Cheong, G. Aeppli, D. A. Tennant, and H. A. Mook, “Softening and Broadening of the Zone Boundary Magnons in $\text{Pr}_{0.63}\text{Sr}_{0.37}\text{MnO}_3$,” *Phys. Rev. Lett.* **80**, 1316–1319 (1998).
- [69] B. Normand, H. Kohno, and H. Fukuyama, “Spin-phonon coupling in the single-layer extended t-J model,” *Phys. Rev. B* **53**, 856–870 (1996).
- [70] Yu. I. Ukhonov, *Optical properties of semiconductors* (Nauka, Moscow, 1977).
- [71] S. Toth and B. Lake, “Linear spin wave theory for single-Q incommensurate magnetic structures,” *J. Phys.: Condens. Matter* **27**, 166002 (2015).

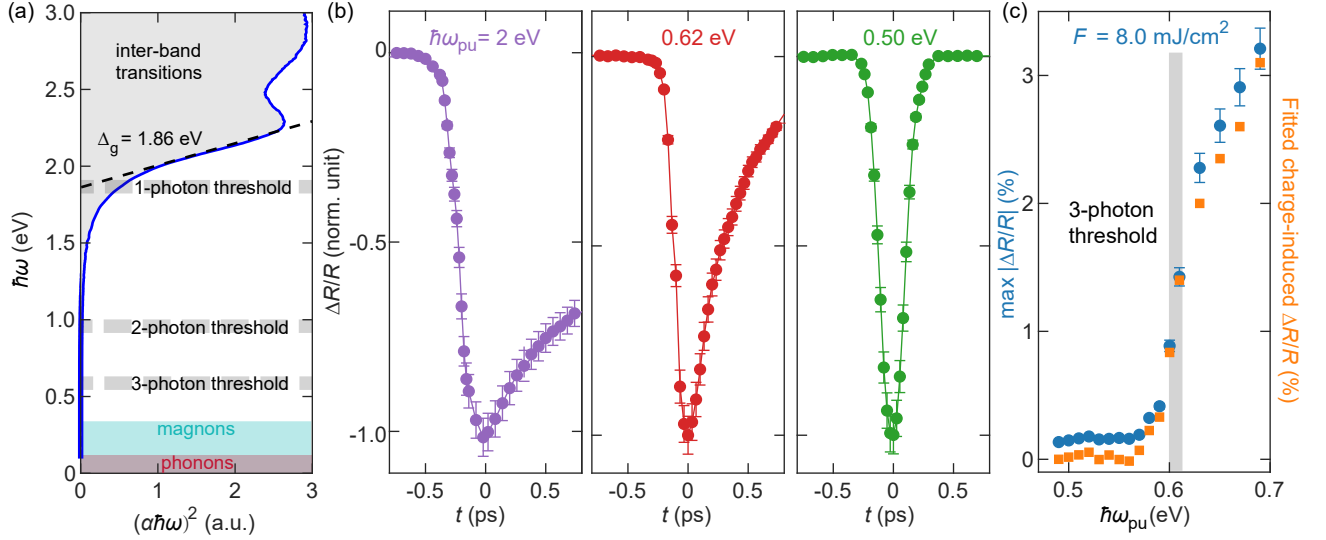


FIG. 1. **Suppressing multiphoton charge excitation in $\text{Sr}_2\text{Cu}_3\text{O}_4\text{Cl}_2$.** (a) Tauc plot (blue curve) for $\text{Sr}_2\text{Cu}_3\text{O}_4\text{Cl}_2$ obtained from ellipsometry measurements taken at $T = 300$ K ($< T_{N,I} = 380$ K), where α is the absorption coefficient and $\hbar\omega$ is the photon energy. Dashed black line is a fit to a general model for inter-band absorption in a three-dimensional insulator [34, 70], yielding $\Delta_g = 1.86$ eV. The energy range of phonons (magnons) is marked by a horizontal red (blue) bar. The threshold energies for 1-, 2- and 3-photon inter-band excitations are marked by dashed gray bars. (b) Normalized $\Delta R/R$ traces at $T = 300$ K for various $\hbar\omega_{pu}$, with $F = 1.4$ mJ/cm², 8.0 mJ/cm² and 8.0 mJ/cm² for the $\hbar\omega_{pu} = 2$ eV, 0.62 eV and 0.50 eV traces, respectively. (c) Maximum ($t = 0$) value of $|\Delta R/R|$, superposed with the amplitude of the photo-carrier contribution to $\Delta R/R$, plotted versus $\hbar\omega_{pu}$ for a fixed $F = 8.0$ mJ/cm². Assuming the 0.50 eV trace is purely coherent, we subtract it from traces taken at other pump photon energies to isolate the photo-carrier contribution to $\Delta R/R$. These background subtracted traces are then fit to an exponential decay function over $0 < t < 700$ fs to extract an amplitude. The gray line denotes the 3-photon threshold. All error bars represent the standard error of the mean from fifteen independent measurements.

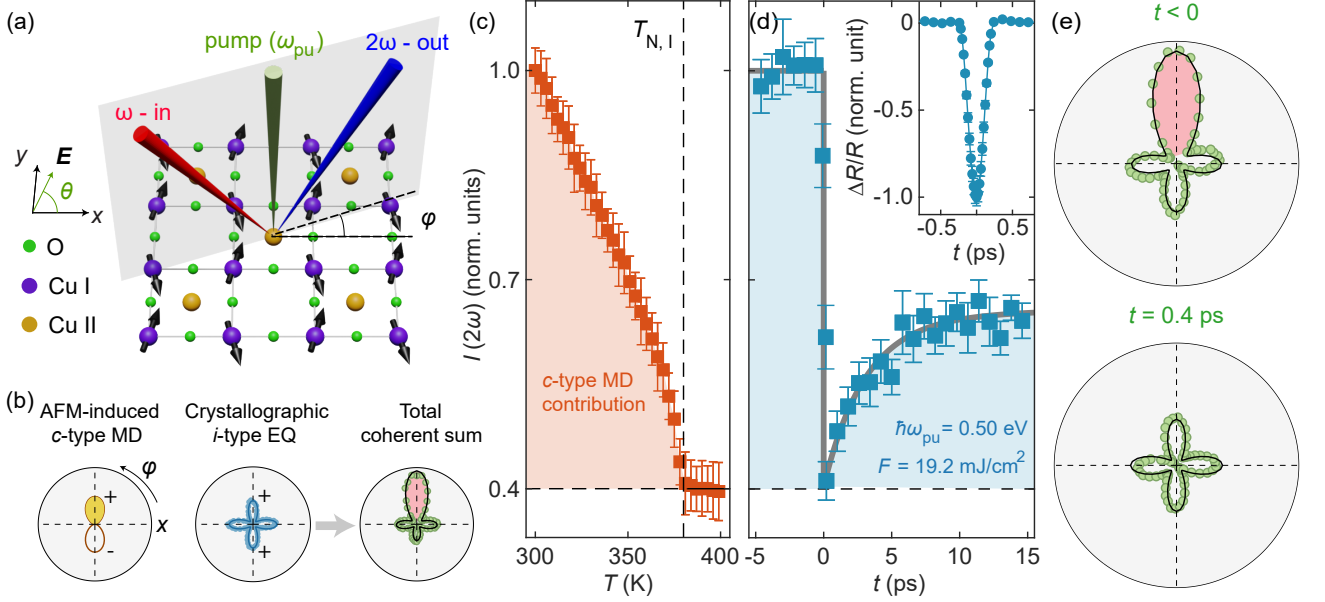


FIG. 2. **Non-thermal magnon-induced magnetic order collapse.** (a) Ordered Cu I spin arrangement (arrows) below $T_{N,I}$. Canting angles are exaggerated for clarity. The probe beam (red) is focused obliquely onto the Cu_3O_4 plane, and the reflected SHG intensity (blue) is measured as a function of the scattering plane angle φ . Both incident and reflected beams are linearly polarized in the scattering plane (gray shade). The pump beam (green) is incident with linear polarization along θ . (b) The *c*-type MD and *i*-type EQ contributions to the RA SHG signal and their coherent sum. Markers in the middle and right panels are the measured RA SHG patterns above (400 K) and below (300 K) $T_{N,I}$, respectively. Solid lines are symmetry-based fits [34]. Different shades in the left panel represent opposite phases. (c) Temperature-dependent static SHG intensity acquired at $\varphi = 90^\circ$ (pink lobe in panel b) normalized to its value at 300 K. The non-magnetic (*i*-type EQ) background value is denoted by a horizontal dashed line. (d) Time-resolved SHG intensity at $\varphi = 90^\circ$ for $\hbar\omega_{\text{pu}} = 0.5$ eV and $F = 19.2$ mJ/cm², plotted on the same scale as panel c. Measurements were taken at $T = 300$ K. Gray line is a guide to the eye. Inset shows $\Delta R/R$ taken with the same pump parameters. All error bars represent the standard error of the mean from four independent measurements. (e) RA SHG data (green circles) measured at $t < 0$ and $t = 0.4$ ps, overlaid with fits to (MD + EQ) and solely EQ contributions, respectively (black curves). We chose $t = 0.4$ ps to represent the instant of maximum demagnetization to avoid coherent artifacts near $t = 0$ [37].

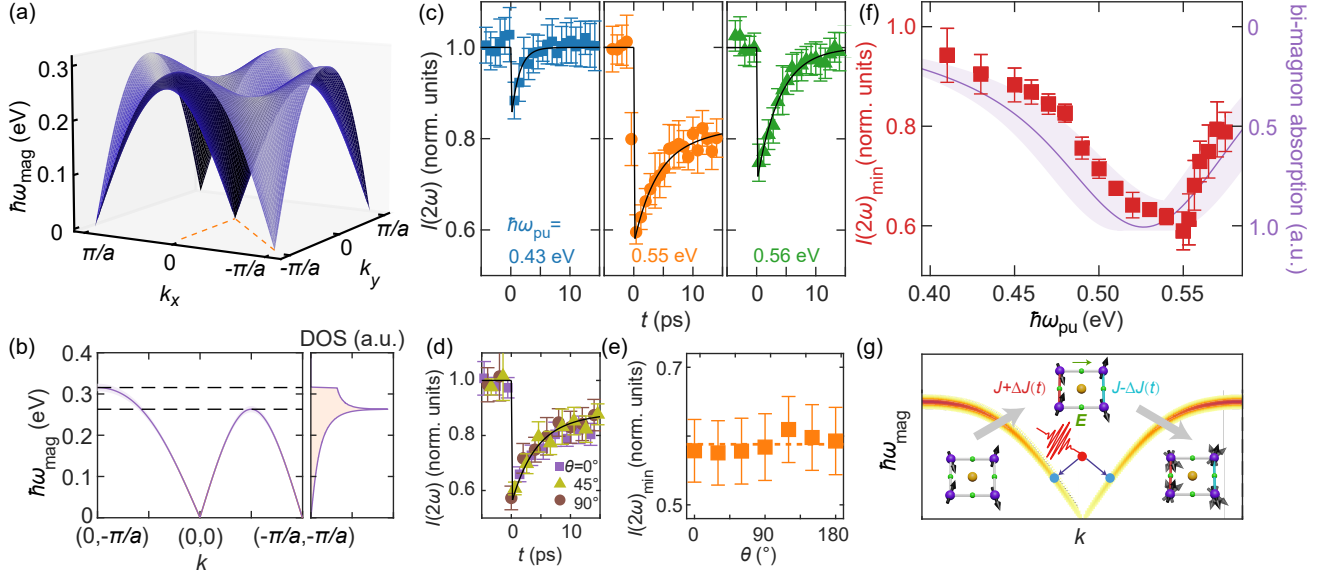


FIG. 3. Parametric magnon pair generation. (a) In-plane ($k_z = 0$) magnon dispersion of the Cu_I sublattice of $\text{Sr}_2\text{Cu}_3\text{O}_4\text{Cl}_2$ calculated using the SpinW code [71] and a J_1 - J_2 model. Values of the nearest- and next nearest-neighbor exchange ($J_1 = 130$ meV, $J_2 = -32.5$ meV) are determined from experiments [32, 42, 43]. The k_x and k_y axes coincide with the x and y directions in Fig. 2a. (b) Magnon dispersion along high-symmetry cuts (dashed line in panel a). The shaded region in the left panel represents the uncertainty in the magnon energy, originating from slight differences in the exchange energies reported in the literature [32, 42, 43]. Horizontal dashed lines indicate van Hove singularities in the magnon density of states (DOS). (c) Transient SHG intensity for select $\hbar\omega_{\text{pu}}$ and fixed $F = 8.0$ mJ/cm². Black lines are guides to the eye. (d) Transient SHG intensity at $t = 0.4$ ps as a function of θ with the same pump conditions as d. (e) Value of the SHG transient at $t = 0.4$ ps as a function of θ with the same pump conditions as d. (f) Value of the SHG transient at $t = 0.4$ ps (red markers) as a function of $\hbar\omega_{\text{pu}}$ for fixed $F = 8.0$ mJ/cm². Purple curve shows the calculated bi-magnon absorption coefficient convolved with a 0.04 eV instrument spectral width. Shaded region represents the range over which the bi-magnon absorption coefficient varies using the range of different magnon energies plotted in panel b. All measurements were taken at $T = 300$ K. All error bars represent the standard error of the mean from four independent measurements. (g) Schematic of the parametric generation process where a photon with energy $\hbar\omega_{\text{pu}}$ converts into a magnon pair with equal energy $\hbar\omega_{\text{mag}} = \hbar\omega_{\text{pu}}/2$ and opposite momentum. Inset: Microscopically, light polarized along the x direction (green arrow) temporally modulates the superexchange along the vertical bonds, with opposite bonds modulated by opposite signs owing to inversion symmetry.

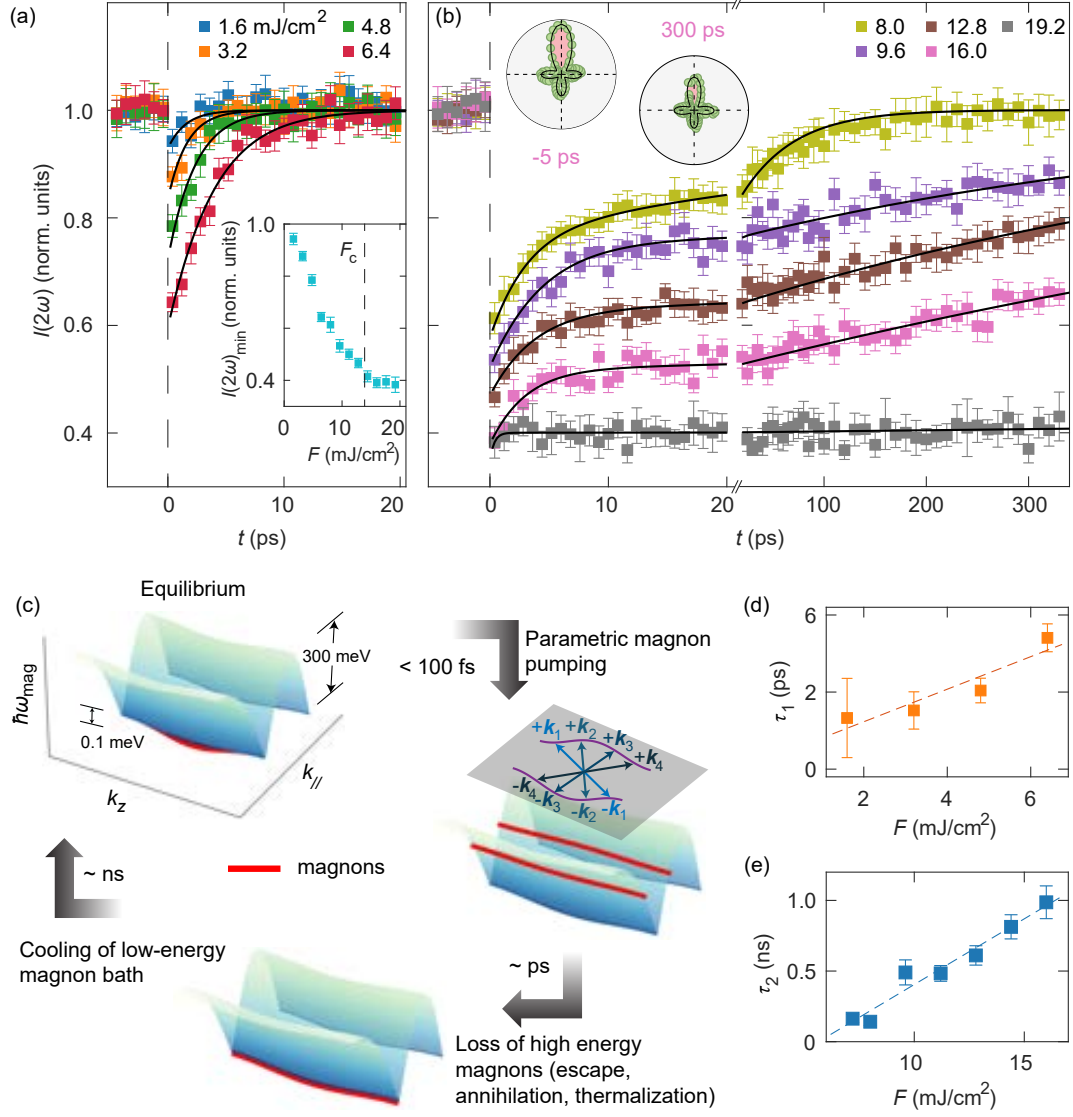


FIG. 4. Out-of-equilibrium relaxation dynamics of the magnon bath. Time-resolved SHG transients measured at $T = 300$ K, $\varphi = 90^\circ$, and $\hbar\omega_{\text{pu}} = 0.55$ eV for select pump fluences in the (a) weak and (b) strong pumping regimes. Fits to a bi-exponential function of the form $\chi_{ijk}^{\text{MD}}(t) = \chi_{ijk}^{\text{MD}}(t < 0) - A_1 \exp(-t/\tau_1) - A_2 \exp(-t/\tau_2)$ are overlaid (black lines). Inset in a shows the fluence dependence of the minimum SHG intensity and the inset in b shows RA SHG patterns at select time delays for $F = 16$ mJ/cm². Error bars represent the standard error of the mean from fifteen independent measurements. Since $\hbar\omega_{\text{pu}} = 0.55$ eV is close to $\Delta_g/3$, we also acquired $\Delta R/R$ traces at this photon energy to check for multiphoton absorption. Slight asymmetry about $t = 0$ was only measurable for fluences above around 12.8 mJ/cm² [34]. (c) Schematic of the multi-stage relaxation process. The magnon dispersion is plotted versus in-plane (k_{\parallel}) and out-of-plane (k_z) momentum. The dispersion along k_z is exaggerated for clarity. The magnon occupation at each stage (red) is overlaid. The gray shaded plane shows different possible momentum combinations of excited magnon pairs. (d) Fitted values of τ_1 and (e) τ_2 as a function of fluence. Error bars represent the fitting uncertainties.

Supplemental Material for

Dynamic magnetic phase transition induced by parametric magnon pumping

Jun-Yi Shan, Jonathan B. Curtis, Mingyao Guo, Chang Jae Roh, C. R. Rotundu, Young S. Lee,
Prineha Narang, Tae Won Noh, Eugene Demler, D. Hsieh

Corresponding author: dhsieh@caltech.edu

Table of contents

- S1. Experimental methods**
- S2. Absorption data at $T = 300$ K**
- S3. Symmetry-based fitting of the static SHG data and magnetic domain identification**
- S4. Ruling out a thermal origin of demagnetization**
- S5. Computing the magnon spectrum**
- S6. Temperature dependence of the demagnetization efficiency**
- S7. Polarization dependence of the magnetic dipolar mechanism**
- S8. Derivation of the parametric excitation**
- S9. Derivation of the bi-magnon absorption coefficient**
- S10. Fitting the pump fluence dependence of τ_2**
- S11. Fluence dependence of $\Delta R/R$ for $\hbar\omega_{pu} = 0.55$ eV**

S1. Experimental methods

Single crystals of $\text{Sr}_2\text{Cu}_3\text{O}_4\text{Cl}_2$ crystals were grown by an optimized method of slow cooling from the melt. Quantities of SrO, SrCl_2 , and CuO powders were mixed in a 1:1:3 stoichiometric ratio and placed in a large high form alumina crucible. The mix was gradually heated in air to 1030 °C, dwelled for 5 h, then cooled to 900 °C at a rate of 2 °C h⁻¹. Placing the crucible in a slight temperature gradient (off-center of the hot chamber of the box furnace) resulted in a centimeter-sized plate-like single crystal. Samples are stable in the air. The high quality of the samples was checked by X-ray diffraction, Laue X-ray, and low-temperature magnetization measurements. Prior to optical measurements, crystals were cleaved along the (001) planes. The results presented in this paper were repeated on four different samples from different growth batches.

We used a Ti:sapphire laser with a repetition rate of 1 kHz. The fundamental output of the laser at 800 nm was used as the probe pulse (80 fs width), which was focused obliquely onto a 60 μm spot on the cleaved surface of the $\text{Sr}_2\text{Cu}_3\text{O}_4\text{Cl}_2$ crystal at a 10° angle of incidence. We checked that the SHG drops are independent of the probe fluence, ranging from 1.4 mJ/cm² to 10 mJ/cm². The $\Delta R/R$ data were measured with a lock-in amplifier. The RA SHG patterns were obtained using a fast-rotating scattering plane based technique¹. Part of the fundamental output was split off to an optical parametric amplifier and a difference frequency generator to serve as the pump pulse (duration 120 fs). The pump pulse was focused normally onto a 110 μm spot on the sample. The penetration depth of the pump beam ($\sim 1 \mu\text{m}$) is much longer than the penetration depth of the SHG beam ($\sim 0.05 \mu\text{m}$), so the probed depth is uniformly pumped. The time-resolved measurements were carried out at 300 K. We did not apply an external magnetic field to the sample. All reported sizes, widths, and durations are full width at half maximum (FWHM).

S2. Absorption data at $T = 300$ K

Fig. S1 shows the absorption coefficient of $\text{Sr}_2\text{Cu}_3\text{O}_4\text{Cl}_2$ below 3 eV, obtained from ellipsometry measurements and the relation $\alpha = 4\pi k/\lambda$, where α is the absorption coefficient, k is the imaginary part of the refractive index, and λ is the wavelength. In the main text, we fit the absorption coefficient data to a general formula for direct allowed transitions in three-dimensional semiconductors², $\alpha(\hbar\omega) = (A/\hbar\omega)\sqrt{\hbar\omega - \Delta_g}\Theta(\hbar\omega - \Delta_g)$, where $\hbar\omega$ is the photon energy, A is a constant, Δ_g is the charge transfer gap energy, and $\Theta(\cdot)$ is the Heaviside function. We can rearrange this formula for the range of $\hbar\omega > \Delta_g$ to $(\alpha\hbar\omega)^2 = A^2(\hbar\omega - \Delta_g)$. Therefore, in Fig. 1a of the main text we plotted $(\alpha\hbar\omega)^2$ as a function of $\hbar\omega$ and performed a linear fit to obtain $\Delta_g = 1.863(3)$ eV.

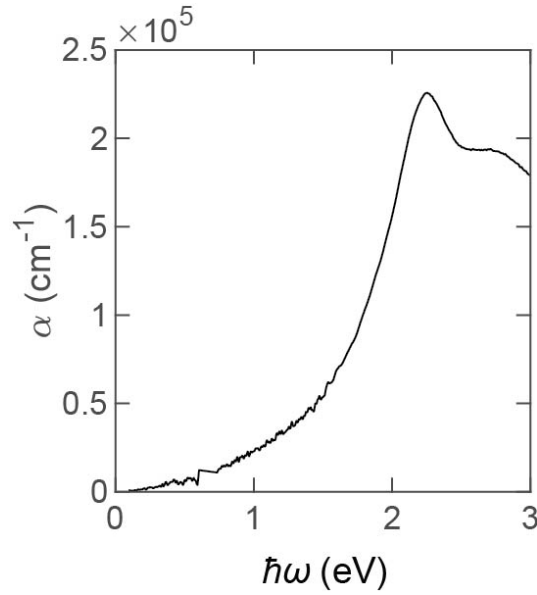


Fig. S1. The absorption coefficient of $\text{Sr}_2\text{Cu}_3\text{O}_4\text{Cl}_2$ at $T = 300$ K.

S3. Symmetry-based fitting of the static SHG data and magnetic domain identification

The crystallographic point group³ of $\text{Sr}_2\text{Cu}_3\text{O}_4\text{Cl}_2$ is centrosymmetric $4/mmm$, which allows bulk electric quadrupole (EQ) SHG of the form $P_i^{\text{EQ}}(2\omega) = \chi_{ijkl}^{\text{EQ}} E_j(\omega)(\partial_k E_l(\omega) + \partial_l E_k(\omega))$, where $P_i^{\text{EQ}}(2\omega)$ is the polarization induced at frequency 2ω , χ_{ijkl}^{EQ} is the EQ SHG susceptibility, and $E(\omega)$ is the incident electric field at frequency ω . The indices i, j, k , and l run over x, y , and z . The symmetry-allowed χ_{ijkl}^{EQ} has 5 independent non-zero elements⁴:

$$\chi^{\text{EQ}} = \begin{pmatrix} \begin{pmatrix} \chi_{xxxx}^{\text{EQ}} & 0 & 0 \\ 0 & \chi_{xyyx}^{\text{EQ}} & 0 \\ 0 & 0 & \chi_{xzzx}^{\text{EQ}} \end{pmatrix} & \begin{pmatrix} 0 & \chi_{xyyx}^{\text{EQ}} & 0 \\ \chi_{xyyx}^{\text{EQ}} & 0 & 0 \\ 0 & 0 & 0 \end{pmatrix} & \begin{pmatrix} 0 & 0 & \chi_{xzzx}^{\text{EQ}} \\ 0 & 0 & 0 \\ \chi_{xzzx}^{\text{EQ}} & 0 & 0 \end{pmatrix} \\ \begin{pmatrix} 0 & \chi_{xyyx}^{\text{EQ}} & 0 \\ \chi_{xyyx}^{\text{EQ}} & 0 & 0 \\ 0 & 0 & 0 \end{pmatrix} & \begin{pmatrix} \chi_{xyyx}^{\text{EQ}} & 0 & 0 \\ 0 & \chi_{xxxx}^{\text{EQ}} & 0 \\ 0 & 0 & \chi_{xzzx}^{\text{EQ}} \end{pmatrix} & \begin{pmatrix} 0 & 0 & 0 \\ 0 & 0 & \chi_{xzzx}^{\text{EQ}} \\ 0 & \chi_{xzzx}^{\text{EQ}} & 0 \end{pmatrix} \\ \begin{pmatrix} 0 & 0 & \chi_{xzzx}^{\text{EQ}} \\ 0 & 0 & 0 \\ \chi_{xzzx}^{\text{EQ}} & 0 & 0 \end{pmatrix} & \begin{pmatrix} 0 & 0 & 0 \\ 0 & 0 & \chi_{xzzx}^{\text{EQ}} \\ 0 & \chi_{xzzx}^{\text{EQ}} & 0 \end{pmatrix} & \begin{pmatrix} \chi_{xzzx}^{\text{EQ}} & 0 & 0 \\ 0 & \chi_{xzzx}^{\text{EQ}} & 0 \\ 0 & 0 & \chi_{xzzx}^{\text{EQ}} \end{pmatrix} \end{pmatrix} \quad (\text{S1})$$

In the polarization channel where the electric fields of both the incident and reflected beams are in the scattering plane, the EQ SHG amplitude has the form of $a+b\cos(4\varphi)$, where φ is the scattering plane angle, and a, b are linear combinations of χ^{EQ} elements.

Below $T_{\text{N,L}}$, the magnetic point group of $\text{Sr}_2\text{Cu}_3\text{O}_4\text{Cl}_2$ is centrosymmetric $mm'm'$, where the macroscopic magnetization is along the x axis. In this phase an additional bulk magnetic dipole (MD) SHG term becomes allowed, described by the equation $P_i^{\text{MD}}(2\omega) = \chi_{ijk}^{\text{MD}} E_j(\omega) H_k(\omega)$, where $H(\omega)$ is the magnetic field at frequency ω . The symmetry-allowed χ_{ijk}^{MD} has 7 independent non-zero elements^{4,5}:

$$\chi^{\text{MD}} = \begin{pmatrix} \begin{pmatrix} \chi_{xxx}^{\text{MD}} & 0 & 0 \\ 0 & \chi_{xyy}^{\text{MD}} & 0 \\ 0 & 0 & \chi_{xzz}^{\text{MD}} \end{pmatrix} \\ \begin{pmatrix} 0 & \chi_{xyy}^{\text{MD}} & 0 \\ \chi_{xyy}^{\text{MD}} & 0 & 0 \\ 0 & 0 & 0 \end{pmatrix} \\ \begin{pmatrix} 0 & 0 & \chi_{xzz}^{\text{MD}} \\ 0 & 0 & 0 \\ \chi_{xzz}^{\text{MD}} & 0 & 0 \end{pmatrix} \end{pmatrix} \quad (\text{S2})$$

In the same polarization channel as above, the MD SHG amplitude has the form of $c\sin\varphi + d\cos^2\varphi\sin(\varphi) + e\sin^3\varphi$, where c, d , and e are linear combinations of χ^{MD} elements. The SHG

rotational anisotropy patterns below $T_{N,I}$ in the main text are fitted as an interference between EQ and MD amplitudes, where the coefficients are complex numbers.

Interference between the EQ and MD terms below $T_{N,I}$ leads to an SHG rotational anisotropy pattern with three small and one large lobe. Different magnetic domains (as large as 1 mm in size) can therefore be distinguished based on the orientation of the large lobe⁵ (Fig. S2). In our experiment, we identified domain boundaries by performing SHG rotational anisotropy measurements at different locations on the sample, and then made sure to focus our pump and probe beams within a single domain.

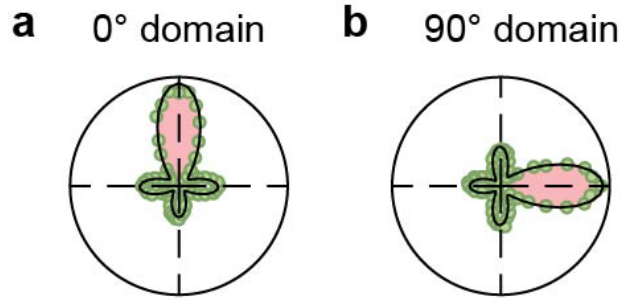


Fig. S2. Static SHG patterns for (a) 0° and (b) 90° magnetic domains measured in the PP polarization channel.

S4. Ruling out a thermal origin of demagnetization

In this section we show that our reported pump-induced demagnetization cannot be explained using a thermal picture⁶.

- 1) Assume the pump pulse energy is initially absorbed by the charge subsystem and is then transferred as heat to the magnon subsystem. Such a scenario would be captured by a two-temperature model, where demagnetization occurs following charge decay. However, this is inconsistent with our observations that there is no measurable charge excitation and that the $\Delta R/R$ and SHG signals drop concurrently on the sub-100 fs timescale.
- 2) If the demagnetization were caused by a hot thermal population of magnons, the magnetic order parameter would recover via cooling of the magnon bath, which would occur through heat exchange with the phonon bath or through thermal diffusion out of the pumped region. These processes are typically slow compared to the ~ 1 picosecond recovery times we observe at low pump fluence. Heat exchange between baths typically happens between several to hundreds of picoseconds⁷⁻¹⁰. To estimate the diffusion timescale for $\text{Sr}_2\text{Cu}_3\text{O}_4\text{Cl}_2$, we calculated the thermal diffusivity $D_{\text{th}} = k/c$, where $k = 15 \text{ W}/(\text{K} \cdot \text{m})$ is the thermal conductivity¹¹ and $c = 1500 \text{ kJ}/(\text{m}^3 \cdot \text{K})$ is the volume specific heat¹². This yields D_{th} of order $10^{-5} \text{ m}^2/\text{s}$, implying a diffusion timescale on the order of microseconds, much longer than what we observed, especially for smaller pump fluences.
- 3) In the scenario where a hot thermal magnon bath cools via heat exchange with a colder thermal phonon bath, the cooling rate should depend on the temperature difference between the two baths, becoming faster as the temperature difference gets larger¹³. This means that the magnetic order parameter recovery time should get shorter as the pump fluence increases. However, we observe the opposite trend.
- 4) If the material demagnetizes because the magnon bath is simply heated above T_N , we expect to see the SHG intensity stay flat at zero over the time during which the temperature remains above T_N , and then quickly recover upon cooling through T_N because the SHG intensity is a steep function of temperature just below T_N . We did not observe such features.
- 5) Finally, the fact that we observe the demagnetization efficiency to peak at 0.55 eV pump photon energy indicates that the initial population of magnons must be peaked at the van Hove singularity - a highly non-thermal scenario.

S5. Computing the magnon spectrum

To obtain the magnon DOS, we modeled the magnon spectrum of Cu_I spins in $\text{Sr}_2\text{Cu}_3\text{O}_4\text{Cl}_2$ using parameters extracted from the following method. Ref. 14 reports the Raman spectra of two closely related 2342 compounds $\text{Ba}_2\text{Cu}_3\text{O}_4\text{Cl}_2$ and $\text{Sr}_2\text{Cu}_3\text{O}_4\text{Cl}_2$, showing their two-magnon peaks lie at very close energies (0.37 eV for $\text{Ba}_2\text{Cu}_3\text{O}_4\text{Cl}_2$ and 0.39 eV for $\text{Sr}_2\text{Cu}_3\text{O}_4\text{Cl}_2$). Therefore, we conclude that the magnetic energy scales of $\text{Ba}_2\text{Cu}_3\text{O}_4\text{Cl}_2$ and $\text{Sr}_2\text{Cu}_3\text{O}_4\text{Cl}_2$ are nearly identical, which is reasonable given the similarity of their structures and the passive roles of the Ba/Sr ions. However, neutron and x-ray scattering are more direct probes of the magnon dispersion relation. Ref. 15 reports neutron scattering data on $\text{Ba}_2\text{Cu}_3\text{O}_4\text{Cl}_2$, showing a saddle point van Hove singularity (vHs) at ~ 0.25 eV, corresponding to twice the saddle point vHs at 0.50 eV. We can then estimate twice the saddle point vHs of $\text{Sr}_2\text{Cu}_3\text{O}_4\text{Cl}_2$ to be 0.51 - 0.54 eV using the reported range of the exchange interactions of the two 2342 compounds^{14,15}.

To model the magnon dispersion of $\text{Sr}_2\text{Cu}_3\text{O}_4\text{Cl}_2$, we adopted a simple J_1 - J_2 model and set $J_1 = 105$ meV and $J_2 = -26.25$ meV to fit the measured ratio of the magnon energies between the maximum and saddle point vHs in the magnon dispersion (i.e., 300 meV/250 meV)¹⁵ and to match the vHs energy of $\text{Sr}_2\text{Cu}_3\text{O}_4\text{Cl}_2$ estimated in the paragraph above. We also sought further confirmation by comparing to a resonant inelastic x-ray scattering (RIXS) measurement¹⁶ of another closely related 2122 compound $\text{Sr}_2\text{CuO}_2\text{Cl}_2$. In $\text{Sr}_2\text{Cu}_3\text{O}_4\text{Cl}_2$ the Cu_I - Cu_{II} interaction is much smaller than the Cu_I - Cu_I interaction³. Therefore, the magnon spectrum of the Cu_I sublattice should be very similar between the 2122 and the 2342 compounds. The magnon dispersion obtained from RIXS on $\text{Sr}_2\text{CuO}_2\text{Cl}_2$ is close to our calculated magnon dispersion, confirming our model.

S6. Temperature dependence of the demagnetization efficiency

To further confirm the non-monotonic behavior of the demagnetization efficiency as a function of the pump photon energy, we measured $I(2\omega)_{\min}$ as a function of $\hbar\omega_{\text{pu}}$ at $T = 110$ K (Fig. S3). We observed the same non-monotonic trend at this lower temperature compared to the $T = 300$ K data, but the peak in efficiency is shifted higher in energy by around 0.01 eV, consistent with the magnon hardening at low temperatures¹⁷.

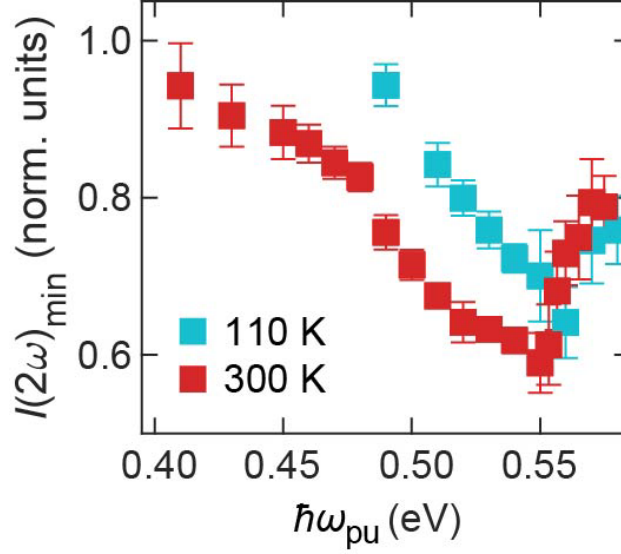


Fig. S3. $I(2\omega)_{\min}$ as a function of $\hbar\omega_{\text{pu}}$ at $T = 110$ K and 300 K with a fixed $F = 8.0$ mJ/cm², normalized to their respective SHG intensity at $t < 0$. The 300 K data are the same as the data presented in Fig. 3f of the main text. All error bars represent the standard error of the mean from four independent measurements.

S7. Polarization dependence of the magnetic dipolar mechanism

The magnetic dipolar interaction H_{m-d} between the magnetic field of the pump beam \mathbf{B}_{pu} and the total spin \mathbf{S} can be written as $H_{m-d} = -\gamma \mathbf{B}_{pu} \cdot \mathbf{S} \cos(\omega_{pu} t)$, where γ is the gyromagnetic ratio. We assume that the Néel order is along the y axis. We define $S_i^+ = S_i^x + iS_i^z$ and $S_i^- = S_i^x - iS_i^z$, and use the Holstein-Primakoff transformation between the spin operators and the bosonic operators of the two antiferromagnetic sublattices within CuI, namely,

for sublattice A with spin up:

$$\begin{aligned} S_i^y &= S - a_i^\dagger a_i \\ S_i^+ &= \sqrt{2S - a_i^\dagger a_i} a_i \\ S_i^- &= a_i^\dagger \sqrt{2S - a_i^\dagger a_i} \end{aligned}$$

for sublattice B with spin down:

$$\begin{aligned} S_j^y &= b_j^\dagger b_j - S \\ S_j^+ &= b_j^\dagger \sqrt{2S - b_j^\dagger b_j} \\ S_j^- &= \sqrt{2S - b_j^\dagger b_j} b_j, \end{aligned}$$

(S3)

where S is the spin quantum number. According to Fig. 2a of the main text, the angle between \mathbf{B}_{pu} and the y axis is θ . Retaining the lowest-order terms in the bosonic operators, we have

$$\begin{aligned} H_{m-d} &= -\gamma B_{pu} \cos \omega_{pu} t [\sum_{i \in A} \cos \theta (S - a_i^\dagger a_i) + \sin \theta \sqrt{\frac{S}{2}} (a_i + a_i^\dagger) + \sum_{j \in B} \cos \theta (b_j^\dagger b_j - \\ &\quad S) + \sin \theta \sqrt{\frac{S}{2}} (b_j^\dagger + b_j)] \end{aligned}$$

(S4)

We note that the $\cos \theta$ terms do not correspond to any magnon generation, and the $\sin \theta$ terms can generate magnon pairs through second-order perturbation theory. Using Fermi's golden rule in second-order perturbation theory, where the transition probability is proportional to the square of the Hamiltonian matrix elements, we derive that under the magnetic dipolar interaction scenario, the magnon excitation rate should scale like $\sin^2 \theta$, which contradicts our data.

S8. Derivation of the parametric excitation

The Hamiltonian describing the coupling of magnons to light is $H_c = -\mathbf{E}_{pu} \cdot \mathbf{P} \cos(\omega_{pu}t)$, where \mathbf{E}_{pu} is the electric field amplitude of the light and \mathbf{P} is the macroscopic electric dipole induced by the electron exchange. Within the photo-assisted spin exchange mechanism, phenomenologically we have¹⁸

$$\mathbf{P} = \sum_{\langle ij \rangle} \mathbf{\Pi}_{ij} \mathbf{S}_i \cdot \mathbf{S}_j \quad (\text{S5})$$

where the sum is over spin \mathbf{S} on neighboring sites i and j and $\mathbf{\Pi}_{ij}$ is the vector coupling strength, whose exact form can be calculated using the wavefunctions of the orbitals involved. We note that $\mathbf{S}_i \cdot \mathbf{S}_j = S_i^x S_j^x + 1/2(S_i^+ S_j^- + S_i^- S_j^+)$. Retaining the lowest-order terms in the bosonic operators, we can rewrite Eqn. S5 as

$$\mathbf{P} = \sum_{\langle ij \rangle} \mathbf{\Pi}_{ij} [(S - a_i^\dagger a_i)(b_j^\dagger b_j - S) + S(a_i b_j + a_i^\dagger b_j^\dagger)] \quad (\text{S6})$$

which we can further simplify using the symmetry of $\mathbf{\Pi}_{ij}$.

Consider a site i within the sublattice A. It has four nearest neighbors of Cu_I, two along the x axis and two along the y axis, which are equally distanced by the Cu_I-Cu_I bond length a . Note that each Cu_I site in Sr₂Cu₃O₄Cl₂ serves as an inversion center and $\mathbf{\Pi}$ transforms as a vector. Therefore, we have $\mathbf{\Pi}_{i,i+ax} = -\mathbf{\Pi}_{i,i-ax} = \mathbf{\Pi}_1$, and $\mathbf{\Pi}_{i,i+ay} = -\mathbf{\Pi}_{i,i-ay} = \mathbf{\Pi}_2$, where \mathbf{x} and \mathbf{y} represent unit vectors along the x and y axes, respectively. Due to the fourfold rotational symmetry of the lattice $\mathbf{\Pi}_1$ and $\mathbf{\Pi}_2$ should be perpendicular to each other and have equal magnitudes Π . Due to mirror symmetries of the lattice, we determine that $\mathbf{\Pi}_1$ is along \mathbf{y} and $\mathbf{\Pi}_2$ is along \mathbf{x} . Therefore, we have $\mathbf{\Pi}_1 = \Pi \mathbf{y}$ and $\mathbf{\Pi}_2 = \Pi \mathbf{x}$.

Note that translational symmetry by a vector $a\mathbf{x}$ or $a\mathbf{y}$ is broken due to the presence of the Cu_{II} lattice, thus enabling a nonzero Π , since otherwise the translational symmetry would also force $\mathbf{\Pi}_{i,i+ax}$ to be equal to $\mathbf{\Pi}_{i,i-ax}$. This relation between the various crystallographic symmetries and the coupling between the spins and electric field, via $\mathbf{\Pi}$, is shown in Fig. S4. Therefore, we can explicitly sum up the terms in Eqn. S6 along different bonds, where many terms cancel each other due to symmetries, and then perform the Fourier transformation to obtain

$$\begin{aligned} \mathbf{P} &= \sum_{\langle ij \rangle} \mathbf{\Pi}_{ij} S(a_i b_j + a_i^\dagger b_j^\dagger) \\ &= S \sum_{i \in A} \mathbf{\Pi}_1 (a_i b_{i+ax} + a_i^\dagger b_{i+ax}^\dagger - a_i b_{i-ax} - a_i^\dagger b_{i-ax}^\dagger) \\ &\quad + \mathbf{\Pi}_2 (a_i b_{i+ay} + a_i^\dagger b_{i+ay}^\dagger - a_i b_{i-ay} - a_i^\dagger b_{i-ay}^\dagger) \\ &= iS \sum_{\mathbf{k}} \gamma_{\mathbf{k}} (a_{\mathbf{k}}^\dagger b_{-\mathbf{k}}^\dagger - a_{\mathbf{k}} b_{-\mathbf{k}}) \end{aligned} \quad (\text{S7})$$

where $\boldsymbol{\gamma}_k = 2 \sin k_x a \mathbf{\Pi}_1 + 2 \sin k_y a \mathbf{\Pi}_2$. Then we can perform the Bogoliubov transformation and convert the bosonic operators a and b to the magnon operators α and β through

$$\begin{pmatrix} a_k \\ b_{-k}^\dagger \end{pmatrix} = \begin{pmatrix} u_k & v_k \\ v_k & u_k \end{pmatrix} \begin{pmatrix} \alpha_k \\ \beta_{-k}^\dagger \end{pmatrix} \quad (\text{S8})$$

where $u_k^2 - v_k^2 = 1$. Therefore, we have

$$\mathbf{P} = iS \sum_{\mathbf{k}} \boldsymbol{\gamma}_k (\alpha_k^\dagger \beta_{-k}^\dagger - \alpha_k \beta_{-k}) \quad (\text{S9})$$

From Eqn. S9 we can see that an overall inversion symmetry of the lattice does not make \mathbf{P} vanish. The full Hamiltonian H contains a static part $H_0 = \sum_{\mathbf{k}} \hbar \omega_{\text{mag}}(\mathbf{k}) (\alpha_k^\dagger \alpha_k + \beta_k^\dagger \beta_k)$ and a time-dependent part $H_c = -iS \sum_{\mathbf{k}} \mathbf{E}_{\text{pu}} \cdot \boldsymbol{\gamma}_k (\alpha_k^\dagger \beta_{-k}^\dagger - \alpha_k \beta_{-k}) \cos(\omega_{\text{pu}} t)$. We now switch to the Heisenberg picture and derive the equations of motion of operators

$$\begin{aligned} \frac{d\alpha_k}{dt} &= \frac{1}{i\hbar} [\alpha_k, H] \\ &= -i\omega_{\text{mag}}(\mathbf{k}) \alpha_k - S \frac{\mathbf{E}_{\text{pu}} \cdot \boldsymbol{\gamma}_k}{\hbar} \beta_{-k}^\dagger \cos(\omega_{\text{pu}} t) \end{aligned} \quad (\text{S10})$$

In the same manner we have

$$\frac{d\beta_{-k}^\dagger}{dt} = i\omega_{\text{mag}}(\mathbf{k}) \beta_{-k}^\dagger - S \frac{\mathbf{E}_{\text{pu}} \cdot \boldsymbol{\gamma}_k}{\hbar} \alpha_k \cos(\omega_{\text{pu}} t) \quad (\text{S11})$$

To solve this equation, we pass to a rotating frame with $\alpha_k = \tilde{\alpha}_k e^{-i\omega_{\text{mag}}(\mathbf{k})t}$ and $\beta_{-k}^\dagger = \tilde{\beta}_{-k}^\dagger e^{i\omega_{\text{mag}}(\mathbf{k})t}$ and get

$$\begin{aligned} \frac{d\tilde{\alpha}_k}{dt} &= -S \frac{\mathbf{E}_{\text{pu}} \cdot \boldsymbol{\gamma}_k}{\hbar} \tilde{\beta}_{-k}^\dagger \cos(\omega_{\text{pu}} t) e^{2i\omega_{\text{mag}}(\mathbf{k})t} \\ \frac{d\tilde{\beta}_{-k}^\dagger}{dt} &= -S \frac{\mathbf{E}_{\text{pu}} \cdot \boldsymbol{\gamma}_k}{\hbar} \tilde{\alpha}_k \cos(\omega_{\text{pu}} t) e^{-2i\omega_{\text{mag}}(\mathbf{k})t} \end{aligned} \quad (\text{S12})$$

Since $\omega_{\text{pu}} = 2\omega_{\text{mag}}(\mathbf{k})$, we can use the rotating-wave approximation and simplify Eqn. S12 to

$$\begin{aligned} \frac{d\tilde{\alpha}_k}{dt} &= -S \frac{\mathbf{E}_{\text{pu}} \cdot \boldsymbol{\gamma}_k}{2\hbar} \tilde{\beta}_{-k}^\dagger \\ \frac{d\tilde{\beta}_{-k}^\dagger}{dt} &= -S \frac{\mathbf{E}_{\text{pu}} \cdot \boldsymbol{\gamma}_k}{2\hbar} \tilde{\alpha}_k \end{aligned} \quad (\text{S13})$$

Therefore, we can solve for $\tilde{\alpha}_k(t) = \frac{\tilde{\alpha}_k(0) + \tilde{\beta}_{-k}^\dagger(0)}{2} e^{-S \frac{\mathbf{E}_{\text{pu}} \cdot \boldsymbol{\gamma}_k}{2\hbar} t} + \frac{\tilde{\alpha}_k(0) - \tilde{\beta}_{-k}^\dagger(0)}{2} e^{S \frac{\mathbf{E}_{\text{pu}} \cdot \boldsymbol{\gamma}_k}{2\hbar} t}$ and get the magnon number at a large time t for the α branch

$$\langle g | \alpha_k^\dagger \alpha_k | g \rangle = \langle g | \tilde{\alpha}_k^\dagger \tilde{\alpha}_k | g \rangle \propto e^{S \frac{E_{pu} \gamma_k}{\hbar} t} \quad (\text{S14})$$

which shows exponential growth. Similarly, we can show the parametric excitation for the β branch. We note that the exponential growth is limited by nonlinear effects, i.e., a damping term proportional to the magnon population¹⁹. Therefore, in the inset of Fig. 4a of the main text we did not observe an exponential relationship between the demagnetization efficiency and the pump fluence.

We emphasize that our parametric excitation mechanism is fundamentally different from the second-order impulsive stimulated Raman scattering (ISRS) mechanism. Our mechanism is resonant pumping of magnons and involves one photon whose energy is resonant with the magnon pair energy. The ISRS mechanism is off-resonant pumping of magnons and involves two photons, whose energy difference is equal to the magnon pair energy. We can safely rule out the ISRS mechanism because the magnon pair energy we excite in $\text{Sr}_2\text{Cu}_3\text{O}_4\text{Cl}_2$ is much higher than the linewidth of our pump pulse. Moreover, we can achieve energy-selective pumping of magnons through our mechanism but not through the ISRS mechanism.

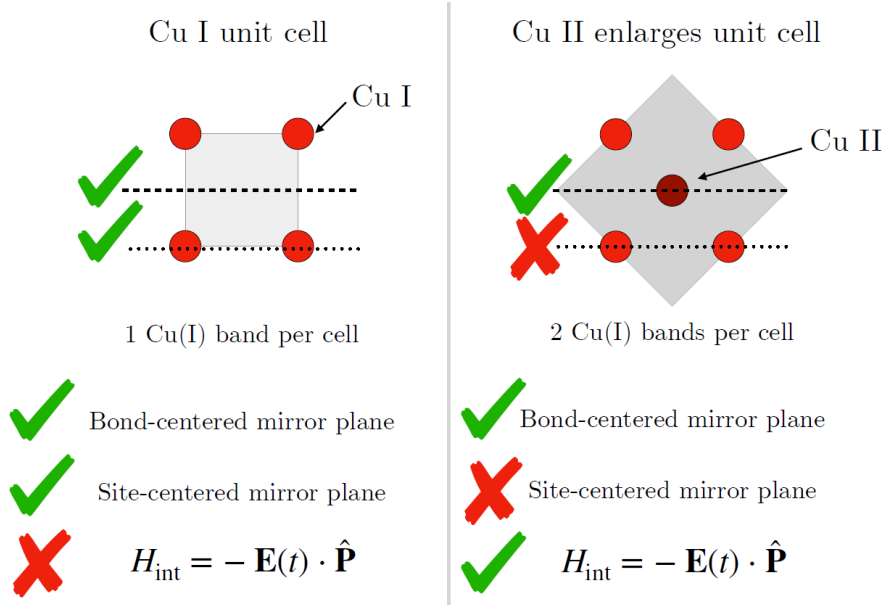


Fig. S4. Local inversion symmetry breaking by Cu II sublattice and its effect on selection rules. With only the Cu I sublattice there is one band per unit cell, and two mirror plane symmetries, forcing the polarization coupling to vanish. In the presence of the Cu II sublattice, there are two bands per unit cell and only one mirror plane survives. This enables odd-parity processes which couple the polarization to the spins.

S9. Derivation of the bi-magnon absorption coefficient

We use Fermi's golden rule to calculate the magnon transition rate Γ to magnons of a specific energy

$$\begin{aligned}\Gamma &= \sum_{\mathbf{k}} \frac{2\pi}{\hbar^2} |\langle 2M(\mathbf{k}) | H_c | g \rangle|^2 \delta(2\hbar\omega_{\text{mag}}(\mathbf{k}) - \hbar\omega_{\text{pu}}) \\ &\propto \frac{2\pi}{\hbar^2} \sum_{2\omega_{\text{mag}}(\mathbf{k})=\omega_{\text{pu}}} (\mathbf{E}_{\text{pu}} \cdot \boldsymbol{\gamma}_{\mathbf{k}})^2 |\langle 2M(\mathbf{k}) | \alpha_{\mathbf{k}}^\dagger \beta_{-\mathbf{k}}^\dagger - \alpha_{\mathbf{k}} \beta_{-\mathbf{k}} | g \rangle|^2\end{aligned}\quad (\text{S15})$$

We note that the state $|2M(\mathbf{k})\rangle$ is the ground state $|g\rangle$ with the creation of magnons in the α and β branches with momenta \mathbf{k} and $-\mathbf{k}$, respectively. Therefore, with a pump photon polarization of \mathbf{e} and a photon energy of $\hbar\omega_{\text{pu}}$, the energy deposited into the magnon system, and thus the bi-magnon absorption coefficient α_{mag} , should be proportional to

$$\begin{aligned}\alpha_{\text{mag}} &\propto \hbar\omega_{\text{pu}} \sum_{2\omega_{\text{mag}}(\mathbf{k})=\omega_{\text{pu}}} (\mathbf{e} \cdot \boldsymbol{\gamma}_{\mathbf{k}})^2 = \Pi \hbar\omega_{\text{pu}} \sum_{2\omega_{\text{mag}}(\mathbf{k})=\omega_{\text{pu}}} (2 \sin k_x a e_y + 2 \sin k_y a e_x)^2 \\ &= \frac{\Pi \hbar\omega_{\text{pu}}}{2} \sum_{2\omega_{\text{mag}}(\mathbf{k})=\omega_{\text{pu}}} [(2 \sin k_x a e_y + 2 \sin k_y a e_x)^2 + (2 \sin k_y a e_y - 2 \sin k_x a e_x)^2]\end{aligned}\quad (\text{S16})$$

The last line is due to the four-fold rotational symmetry. As a result,

$$\alpha_{\text{mag}} \propto \hbar\omega_{\text{pu}} \sum_{2\omega_{\text{mag}}(\mathbf{k})=\omega_{\text{pu}}} (\sin^2 k_x a + \sin^2 k_y a) \quad (\text{S17})$$

which shows an isotropic absorption that does not depend on \mathbf{e} and yields the plot in Fig. 3f of the main text.

While this phenomenological analysis agrees well with experimental observations, it does not uniquely pin down the microscopic origin of this coupling described in Eqn. 2 of the main text. One possible mechanism is that the electric field may excite phonon modes associated to ligand motion. In the presence of the Cu_{II} sublattice, the crystal-field environment of the $\text{Cu}_{\text{I}}\text{-O-Cu}_{\text{I}}$ bond is asymmetric, and the oxygen is expected to buckle slightly away from a linear geometry^{20,21} (Fig. S5a). With light illumination, e.g., polarized in the x direction, the electric field can induce an infrared active phonon mode which displaces the two oxygen ions on the two vertical bonds in the same direction, therefore amplifying the buckling angle of one bond while weakening the buckling angle of the opposite bond. Through superexchange interaction, the spin coupling J_1 is periodically modified, resulting in the coupling as in Eqn. 2 of the main text. However, this mechanism involves coupling of a photon to an infrared active phonon mode. For pump energies far off resonant from any phonon absorption lines, this will be strongly suppressed.

An alternative mechanism is the direct modulation of the electronic hopping. In the presence of the buckled bond geometry, it is expected that the effective Cu_I - Cu_I hopping obtained by integrating out the excited O p -band will also exhibit a dependence on the perpendicular electric field (Fig. S5b), yielding a similar result as the phonon mechanism. Another possible hopping route Cu_I - Cu_II - Cu_I , which does not rely on bond buckling, is also similarly renormalized by the electric field.

We note that in Fig. 3f of the main text, the trend of the demagnetization efficiency as a function of $\hbar\omega_\text{pu}$ agrees well quantitatively with the trend of the bi-magnon absorption spectrum. However, we prefer not to claim quantitative agreement in the value of $\hbar\omega_\text{pu}$ where these two curves achieve their maxima. Any quantitative discrepancy, if it exists, could be attributed to a Raman active phonon excited together with the magnon pair, such as the buckling phonon with an energy of ~ 40 meV^{14,22}.

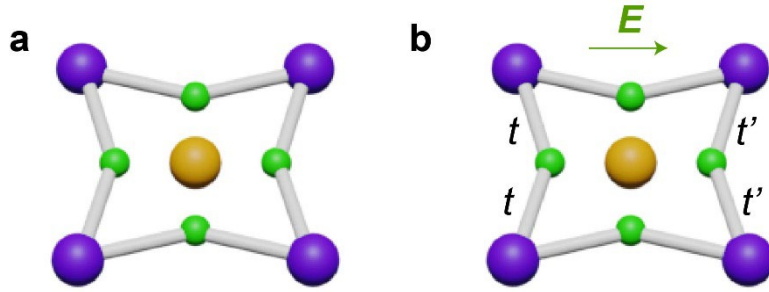


Fig. S5. **a**, Illustration of the Cu_I -O- Cu_I bond buckling. The buckling angle is exaggerated. **b**, Illustration of the hopping modulation. An electric field (E) along the x axis will modulate the vertical Cu_I -O hopping (t and t'), depending on whether the hopping has a component along or against the field direction. Other hopping pathways such as Cu_I - Cu_II - Cu_I are similarly renormalized but are not shown for clarity.

S10. Fitting the pump fluence dependence of τ_2

In Fig. S6 we show the relationship between the fitted τ_2 and the pump fluence F over a wide fluence range. We note that for the three highest fluence data points, the fitted τ_2 is much larger than the time window we used for fitting ($0 < t < 350$ ps), so the error bars (not shown) are very large. We note a possible divergence of τ_2 at large fluence, which can be fit to the functional form $\tau_2 = \tau (1 - F/F^*)^{-1}$, where τ is a phenomenological constant, with a fitted critical fluence of $F^* = 20$ mJ/cm². Such a divergence has previously been reported in photo-doped Sr₂IrO₄ (a layered Mott antiferromagnet) and attributed to critical slowing down across a quasi-thermal magnetic phase transition¹³. However, in our case, further verification of this mechanism would require taking data with much longer time delays.

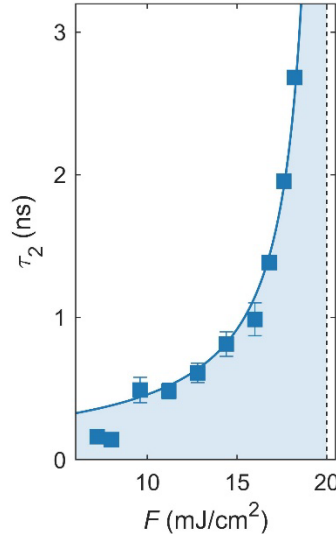


Fig. S6. Fitted values of τ_2 as a function of pump fluence. The solid curve is a fitting to the model $\tau_2 = \tau (1 - F/F^*)^{-1}$.

S11. Fluence dependence of $\Delta R/R$ for $\hbar\omega_{pu} = 0.55$ eV

Figure S7 shows $\Delta R/R$ transients taken under the same experimental conditions as the data in Figs. 4a & b of the main text. Since 0.55 eV is very close to the 3-photon threshold, some asymmetry in the $\Delta R/R$ curves about $t = 0$ begins to develop above around $F > 12.8$ mJ/cm², suggesting some finite three-photon absorption. These photo-carriers can excite magnons upon decay, which add to the population of non-thermal magnons that are directly generated by parametric driving.

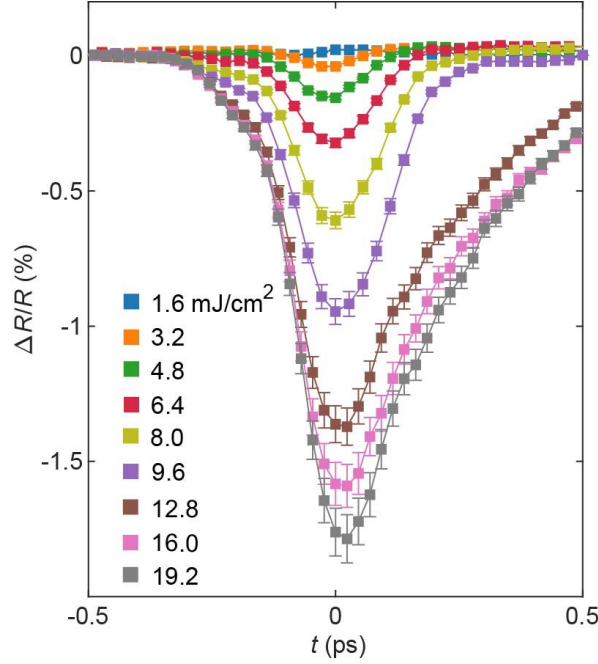


Fig. S7. $\Delta R/R$ transients for $\hbar\omega_{pu} = 0.55$ eV at selected pump fluences. Error bars represent the standard error of the mean from fifteen independent measurements.

References

1. J. W. Harter et al., High-speed measurement of rotational anisotropy nonlinear optical harmonic generation using position-sensitive detection. *Opt. Lett.* **40**, 4671 (2015).
2. Iu I. Ukhanov, Optical properties of semiconductors. Mosc. Izd. Nauka (1977).
3. Y. J. Kim et al., Neutron scattering study of $\text{Sr}_2\text{Cu}_3\text{O}_4\text{Cl}_2$. *Phys. Rev. B* **64**, 024435 (2001).
4. R. W. Boyd, *Nonlinear Optics*. (Academic Press, 2020).
5. K. L. Seyler et al., Direct visualization and control of antiferromagnetic domains and spin reorientation in a parent cuprate. *Phys. Rev. B* **106**, L140403 (2022).
6. A. Kirilyuk et al., Ultrafast optical manipulation of magnetic order. *Rev. Mod. Phys.* **82**, 2731 (2010).
7. A. V. Kimel, R. V. Pisarev, J. Hohlfeld, and Th. Rasing, Ultrafast quenching of the antiferromagnetic order in FeBO_3 : Direct optical probing of the phonon-magnon coupling. *Phys. Rev. Lett.* **89**, 287401 (2002).
8. A. V. Kimel et al., Optical excitation of antiferromagnetic resonance in TmFe_3 . *Phys. Rev. B* **74**, 060403 (2006).
9. M. Matsubara, Y. Okimoto, T. Ogasawara, Y. Tomioka, H. Okamoto, and Y. Tokura, Ultrafast photoinduced insulator-ferromagnet transition in the perovskite manganite $\text{Gd}_{0.55}\text{Sr}_{0.45}\text{MnO}_3$. *Phys. Rev. Lett.* **99**, 207401 (2007).
10. H. Yada et al., Discrimination between photodoping- and heat-induced magnetization changes in $\text{Nd}_{0.52}\text{Sr}_{0.48}\text{MnO}_3$ using a heterostructure with SrTiO_3 . *Phys. Rev. B* **84**, 045114 (2011).
11. M. Ohno et al., Thermal Conductivity due to Spins in the Two-Dimensional Spin System $\text{Ba}_2\text{Cu}_3\text{O}_4\text{Cl}_2$. *J. Phys. Soc. Jpn.* **88**, 064708 (2019).
12. S. Noro et al., Magnetic properties of $\text{Ba}_{2-x}\text{K}_x\text{Cu}_3\text{O}_4\text{Cl}_2$. *Solid State Commun.* **76**, 711 (1990).
13. A. de la Torre et al., Decoupling of static and dynamic criticality in a driven Mott insulator. *Commun. Phys.* **5**, 35 (2022).
14. J. Holmlund et al., Two-magnon Raman scattering from the Cu_3O_4 layers in $(\text{Sr}_2, \text{Ba}_2)\text{Cu}_3\text{O}_4\text{Cl}_2$. *Phys. Rev. B* **79**, 085109 (2009).
15. P. Babkevich et al., Magnetic excitations from the two-dimensional interpenetrating Cu framework in $\text{Ba}_2\text{Cu}_3\text{O}_4\text{Cl}_2$. *Phys. Rev. B* **96**, 014410 (2017).
16. M. Guarise et al., Measurement of magnetic excitations in the two-dimensional antiferromagnetic $\text{Sr}_2\text{CuO}_2\text{Cl}_2$ insulator using resonant x-ray scattering: Evidence for extended interactions. *Phys. Rev. Lett.* **105**, 157006 (2010).
17. H. Y. Hwang et al., Softening and Broadening of the Zone Boundary Magnons in $\text{Pr}_{0.63}\text{Sr}_{0.37}\text{MnO}_3$. *Phys. Rev. Lett.* **80**, 1316 (1998).
18. Y. Tanabe, T. Moriya, and S. Sugano, Magnon-Induced Electric Dipole Transition Moment. *Phys. Rev. Lett.* **15**, 1023–1025 (1965).
19. D. Malz, K. Johannes, and A. Nunnenkamp, Topological magnon amplification. *Nat. Commun.* **10**, 3937 (2019).
20. B. Normand, H. Kohno, and H. Fukuyama, Spin-phonon coupling in the single-layer extended t-J model. *Phys. Rev. B* **53**, 856–870 (1996).
21. J. B. Curtis et al., Cavity magnon-polaritons in cuprate parent compounds. *Phys. Rev. Res.* **4**, 013101 (2022).

22. A. Zibold et al., Optical properties of single-crystal $\text{Sr}_2\text{CuO}_2\text{Cl}_2$. Phys. Rev. B **53**, 11734–11743 (1996).